PAPER • OPEN ACCESS

SOLPS-ITER predictive simulations of the impact of ion-molecule elastic collisions on strongly detached MAST-U Super-X divertor conditions

OPEN ACCESS
IOP Publishing | International Atomic Energy Agency
Nuclear Fusion
Nucl. Fusion **63** (2023) 076030 (20pp)
https://doi.org/10.1088/1741-4326/acd9da

SOLPS-ITER predictive simulations of the impact of ion-molecule elastic collisions on strongly detached MAST-U Super-X divertor conditions

O. Myatra[1,2,*], D. Moulton[1], B. Dudson[2], B. Lipschultz[2], S. Newton[1], K. Verhaegh[1] and A. Fil[1]

[1] UKAEA-CCFE, Culham Science Centre, Abingdon OX14 3DB, United Kingdom of Great Britain and Northern Ireland
[2] York Plasma Institute, University of York, Heslington, York YO10 5DQ, United Kingdom of Great Britain and Northern Ireland

E-mail: omkar.myatra@ukaea.uk

Received 21 October 2022, revised 25 April 2023
Accepted for publication 30 May 2023
Published 19 June 2023

Abstract

The role of ion-molecule ($D^+ - D_2$) elastic collisions in strongly detached divertor conditions has been studied in the MAST-U Super-X configuration using SOLPS-ITER. Two strongly detached steady state solutions were compared, one obtained through a main-ion fuelling scan and the other through a nitrogen seeding scan at fixed fuelling rate. A significant difference in the electron–ion recombination (EIR) levels was observed; significant EIR in strongly detached conditions in the fuelling scan and negligible EIR throughout the seeding scan. This is partly because the fuelling scan achieves electron temperatures (T_e) as low as 0.2 eV near the divertor target, compared to 0.8 eV in the seeding scan (EIR increases strongly below $T_e \approx 1$ eV), and partly due to higher divertor plasma densities achieved in fuelling scan. Features of the strongly detached seeded cases, i.e. higher temperatures and negligible EIR, are recovered in the fuelling scan by turning off $D^+ - D_2$ elastic collisions. Analysis suggests that dissipation mechanisms like line radiation and charge exchange (important for detachment initiation) become weak when T_e falls below 1 eV, and that $D^+ - D_2$ elastic collisions are necessary for further heat dissipation and access to strongly recombining conditions in the fuelling scan. In the seeding scan, heat dissipation through $D^+ - D_2$ elastic collisions is weak. This could be because our nitrogen seeding simulations do not include interactions between nitrogen ions and neutrals, and the strongly detached cases contain high levels of N^+ in the divertor. As a result, the N^+ acts like a reservoir of energy and momentum which appears to weaken the impact of $D^+ - D_2$ elastic collisions on the divertor plasma energy and momentum balance, making it more difficult to access recombining conditions. This suggests that some of the differences between seeding and fuelling scans could be because energy and momentum exchange between impurities and neutrals is not sufficiently captured in our simulations.

* Author to whom any correspondence should be addressed.

Keywords: tokamak divertor, detachment, molecules, elastic collisions, MAST-U, Super-X, SOLPS-ITER

(Some figures may appear in colour only in the online journal)

1. Introduction

A number of competing goals complicate the operation of nuclear fusion tokamak reactors. Divertor power dissipation through detachment is maximised for high outboard midplane densities and divertor/scrape-off layer (SOL) impurity levels [1–3], whereas maximal core energy confinement is achieved for low pedestal densities [4]. While the impact of impurities on core energy confinement is rather complex—with improved confinement, degraded confinement, as well as no significant impact on confinement reported in a number of studies [5–13]—it is desirable, especially for future high power devices, to minimise the impurity levels in the core as this results in the dilution of the fusion fuel which lowers the core performance [14, 15]. In future high power devices like ITER and DEMO, radiative power dissipation through extrinsic impurities will be required to access detachment and reduce divertor heat loads to acceptable levels [16, 17]. The Super-X divertor (SXD) configuration has been proposed as a solution because of its potential to provide access to detachment at lower midplane separatrix densities and impurity levels, making detached operation more compatible with high core performance. This configuration has been implemented in the MAST Upgrade (MAST-U) tokamak. Previous predictive detachment modelling of MAST-U has primarily focussed on the advantages of the SXD configuration over the conventional divertor configuration [18–21]. This work primarily builds on and extends the predictive modelling presented in [19–21]. We take a closer look at the SXD configuration in MAST-U, and study strongly (and similarly) detached solutions obtained from two different approaches in this study.

Detached divertor conditions are usually studied in experiment through one of two approaches. In so-called 'density ramp' experiments, the plasma fuelling rate is steadily increased, leading to an increase in the outboard midplane density, resulting in higher divertor densities and lower divertor temperatures, conducive to detachment. While no impurities are injected, intrinsic impurities are present in the plasma due to erosion of plasma facing components, which may lead to significant radiative losses in carbon devices. In the second approach, the core line-integrated density (and therefore the outboard midplane density) is held roughly constant, while extrinsic impurities are added or 'seeded' in the plasma, with injection rate increasing with time so as to radiatively dissipate heat in the divertor and access divertor detachment through lower plasma temperatures.

Strongly detached divertor conditions have been observed to vary significantly across devices and often depend on the approach taken to access detachment. An important experimental characteristic of detachment is the drop in target ion current density or the total integrated ion flux to the target, $\Gamma_{t,ion}$. In density ramp experiments, volumetric electron–ion recombination (EIR—dielectric and three-body recombination), which occurs at $T_e < 1.5$ eV, can be non-negligible at detachment onset, and can account for a large fraction (up to 75%) of the reduction in $\Gamma_{t,ion}$ in strongly detached conditions as observed in Alcator C-Mod [22]. It is also possible for the role of EIR to be small in density ramp experiments as in Tokamak à configuration variable (TCV) [23] (negligible at detachment onset and increasing to 10%–15% at similar detachment levels as in C-Mod). In experiments in which impurities are injected to achieve detachment, EIR typically has a much smaller role in bringing down $\Gamma_{t,ion}$. In C-Mod, the reduction in $\Gamma_{t,ion}$ due to EIR drops from 75% during a density ramp to ≈10% with N_2-seeding to achieve detachment [24]. Similarly, the role of EIR in TCV drops from small (10%–15%) during a density ramp to below measurable [23] for similarly detached N_2-seeded discharges. In addition to EIR, ions can be volumetrically recombined through a chain of plasma-molecular interaction processes, resulting in molecular activated recombination (MAR). MAR is expected to occur at higher temperatures than EIR ($T_e \approx 1-3$ eV). Although EIR is small for TCV, MAR can account for up to half of the reduction of $\Gamma_{t,ion}$ on TCV during density ramps [25]. Analysis of N_2 seeded discharges, however, indicated negligible levels of MAR. The ion load to the target, which is reduced during detachment and which facilitates large heat flux reductions as the surface recombination heat load is reduced, can also be lowered by a reduction of the divertor ion source. TCV studies [23] indicate that this ion source reduction could explain the reduction of the ion target flux during seeded conditions. It should be noted that we are not suggesting any kind of initial value effect. We are not saying that through seeding, one can get to different divertor target conditions for the same upstream conditions as when using the density ramp approach—we are just saying that we get to different points in the impurity concentration and midplane density space by fuelling compared to seeding, and these different points have different target properties.

In this study, we have used the SOLPS-ITER code package [26] to investigate differences between detached states achieved using these two different approaches to detachment in the MAST-U SXD configuration. We have chosen nitrogen for the seeded impurity while carbon is the intrinsic impurity for both methods. Strongly detached steady state solutions are achieved through the use of either method.

The aim was to carry out a detailed comparison of conditions when the divertor is detached due to a high upstream density to those when it is a result of significantly increased

impurity radiation in the divertor at a relatively low upstream density. Consistent with experimental observations in other tokamaks, we find that EIR plays a significant role in reducing $\Gamma_{t,ion}$ in strongly detached solutions obtained from the fuelling scan. In the seeding scan, $\Gamma_{t,ion}$ is roughly equal to the divertor integrated ionisation source for all seeding rates due to negligible EIR even in strongly detached solutions. We find that MAR does not play a significant role in our simulations. However, we note that MAR (as well as molecular activated dissociation—MAD), involving D_2^+, may be underestimated in SOLPS-ITER as the reaction rates are specified for hydrogen and in certain cases re-scaled to deuterium using a simplified mass re-scaling [27, 28]. As one would expect, a higher divertor electron density and lower plasma temperature near the target is achieved in the fuelling scan. Following an energy, momentum and particle balance analysis of the divertor plasma, it was hypothesized that qualitative features of the nitrogen seeded detached divertor (lower/higher density/temperature and thus little EIR) may be recovered in the non-seeded case by excluding $D^+ - D_2$ elastic collisions in the model. This hypothesis was confirmed after repeating the fuelling scan with $D^+ - D_2$ elastic collisions excluded: lower divertor densities and higher divertor target temperatures were achieved and EIR dropped to negligible levels for similar upstream conditions when this interaction was turned off, demonstrating that in our simulations (for the chosen set of plasma-neutral interactions and available reaction rates), it is this interaction that leads to lower electron temperatures and higher electron densities, providing a pathway to strong EIR conditions in the fuelling scan.

The focus of this paper is to discuss how (in SOLPS) $D^+ - D_2$ elastic collisions provide access to lower temperature/higher density conditions relevant for EIR in the fuelling scan; and possible reasons why they have a weak impact on the divertor energy/momentum balance in the seeded scan. All quantitative plots in this work originate from SOLPS predictive simulations of MAST-U scans, some of which (e.g. nitrogen seeding) have not yet been performed in experiment. In the next section, the simulation setup for the three scans and the observed differences in the role of EIR in reducing $\Gamma_{t,ion}$ are described. A strongly detached case from each scan is compared in section 3, various features of the plasma solutions and the energy, momentum and particle balance in the divertor are discussed in detail. Conclusions are summarised in section 4.

2. Detached solutions obtained with SOLPS-ITER

2.1. Simulation setup

Since this work is an extension the predictive modelling presented in [19–21], we have used essentially the same physics model: the code was run with neutral-neutral collisions, impurity neutralisation and drifts turned off, and we do not solve for parallel currents in the SOL (no potential equation). The plasma simulation domain is shown in figure 1(*a*), it corresponds to a SXD equilibrium similar to the ones used in [20, 21]. In this geometry, three parameter scans were performed for a fixed power entering the core boundary. Two of these were fuelling scans in which D_2 molecules were injected from the inboard midplane (figure 1(*a*)). The third scan is the impurity seeding scan in which nitrogen atoms (N) are injected into the divertor, close to the entrance (up-down symmetric, figure 1(*a*)). In each scan, steady state solutions are obtained for each fuelling or seeding rate.

SOLPS-ITER makes use of the AMJUEL database [29], which contains reaction rates for various plasma-neutral interactions. The ones used in this study are shown in table 1. The nitrogen seeding scan includes all the plasma-neutral interactions shown in table 1. Since there is no nitrogen in the D_2 fuelling scans, nitrogen ionisation (AMJUEL H.4,10 2.7A0) is not included in these scans. As mentioned earlier, elastic collisions between ions and molecules (AMJUEL H.0,1,3 0.3 T) are excluded in one of the fuelling scans. The only other way for deuterium ions (D^+) to interact with deuterium molecules in these simulations is through ion-conversion (molecular charge-exchange, AMJUEL H.2 3.2.3), which is included in all three scans. The fuelling rate is varied from $1 \times 10^{21} - 1.1 \times 10^{22}$ D nuclei s^{-1} for the case with $D^+ - D_2$ elastic collisions and from $1 \times 10^{21} - 8 \times 10^{21}$ D nuclei s^{-1} for the case without. For the nitrogen seeding scan, a case that is at the threshold of ion flux roll-over is chosen from the fuelling scan (which includes $D^+ - D_2$ elastic collisions, fuelling rate $= 2 \times 10^{21}$ D nuclei s^{-1}) and the nitrogen seeding rate is varied from $5 \times 10^{19} - 1.1 \times 10^{21}$ N nuclei s^{-1}. Nitrogen chemistry (e.g. ammonia production) and molecules are treated in SOLPS-ITER using the AMMONX database [30], which contains the corresponding reaction rates. However, to maintain connection with previous work [19], nitrogen chemistry and molecules are not included in these simulations. Intrinsic carbon is included as a sputtered impurity in all scans, with 3% chemical sputtering yield as in previous MAST-U studies [20, 21].

The plasma boundary conditions chosen in these simulations are identical to the ones presented in [21]. The total power entering the domain through the core boundary is 2.5 MW in each scan. The pumping speed is set to 10.7 $m^3\,s^{-1}$, and the deuterium and carbon recycling fractions are set to 1 and 0 respectively in as done in [20, 21] (for both ions and neutrals). Previous interpretive modelling of TCV discharges, which also compares upstream density driven and nitrogen seeding driven detachment, has estimated the nitrogen recycling fraction to be between 0.3 and 0.5 [31]. In this work, however, we have used a nitrogen recycling fraction of 1 as done in previous predictive modelling [19] and since there is currently no corresponding data from MAST-U. Nitrogen neutrals are recycled as atoms, and deuterium neutrals (atoms and molecules) are recycled as molecules. All species are recycled at wall temperature (300 K). In all cases, the cross-field heat diffusivity, $\chi_\perp = 10$ $m^2\,s^{-1}$ and particle diffusivity, $D_\perp = 0.2$ $m^2\,s^{-1}$ are used for the main chamber (SOL above the X-point as well as the core) except in a small region inside the core where, to emulate H-mode temperature and density

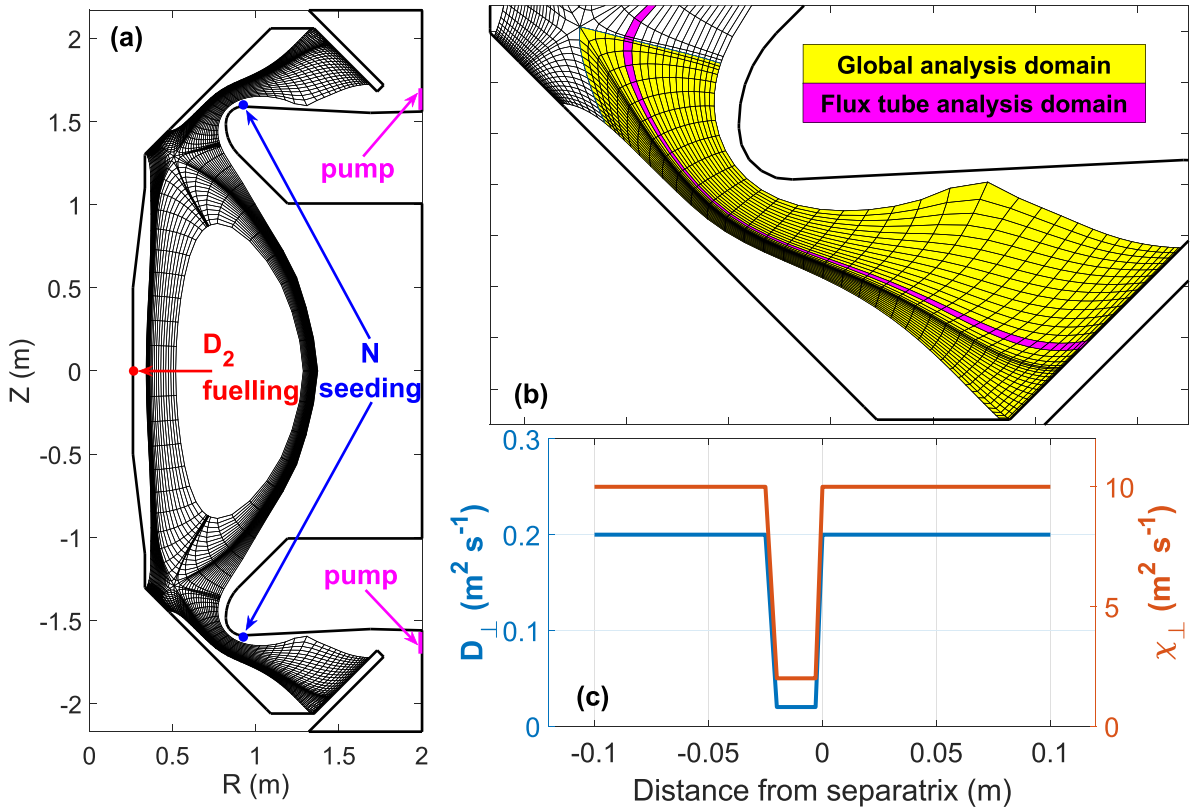

Figure 1. (*a*) Plasma domain (*b*) global and flux tube analysis domains (*c*) radial profiles of $\chi_\perp$ and $D_\perp$.

Table 1. EIRENE reactions included. Note that the EIRENE / AMJUEL reaction rates are specified for hydrogen and in certain cases are re-scaled to deuterium using a simplified mass re-scaling [27]. In the case of H.2 3.2.3, this can result in an underestimation of the cross-section, especially at detachment-relevant temperatures [25, 28].

Database and reaction code	Reaction
AMJUEL H.4,10 2.1.5	$D + e \rightarrow D^+ + 2e$
AMJUEL H.4,10 2.6A0	$C + e \rightarrow C^+ + 2e$
AMJUEL H.4,10 2.7A0	$N + e \rightarrow N^+ + 2e$
AMJUEL H.4 2.2.9	$D_2 + e \rightarrow D_2^+ + 2e$
AMJUEL H.4 2.2.5 g	$D_2 + e \rightarrow 2D + e$
AMJUEL H.4 2.2.10	$D_2 + e \rightarrow D + D^+ + 2e$
AMJUEL H.4 2.2.11	$D_2^+ + e \rightarrow 2D^+ + 2e$
AMJUEL H.4 2.2.12	$D_2^+ + e \rightarrow D + D^+ + e$
HYDHEL H.1,3 3.1.8	$D + D^+ \rightarrow D^+ + D$
METHANE H.1,3 3.2	$D^+ + C \rightarrow C^+ + D$
AMJUEL H.2 3.2.3	$D_2 + D^+ \rightarrow D + D_2^+$
AMJUEL H.0,1,3 0.3 T	$D_2 + D^+ \rightarrow D_2 + D^+$
AMJUEL H.4,8 2.2.14	$D_2^+ + e \rightarrow D + D$
AMJUEL H.4,10 2.1.8	$D^+ + e \rightarrow D$
AMJUEL H.4,10 2.1.8	$D^+ + 2e \rightarrow D + e$

pedestals, we have used $\chi_\perp = 2\,\mathrm{m^2\,s^{-1}}$ and $D_\perp = 0.02\,\mathrm{m^2\,s^{-1}}$ (figure 1(*c*)). These diffusivities have been used in [21] and give radial SOL decay widths of power $\lambda_q \approx 7.5\,\mathrm{mm}$, and plasma density and temperature $\lambda_{n_e} = \lambda_{T_e} \approx 16\,\mathrm{mm}$ respectively, similar to values found in MAST H-mode experiments [32–34]. The radial resolution of our grid at the outboard midplane is such that we have eight points between the separatrix and the first λ_q. Below the X-point (divetor SOLs and private flux regions), we set $D_\perp = \chi_\perp = 1\,\mathrm{m^2\,s^{-1}}$ in accordance with previous work [20, 21].

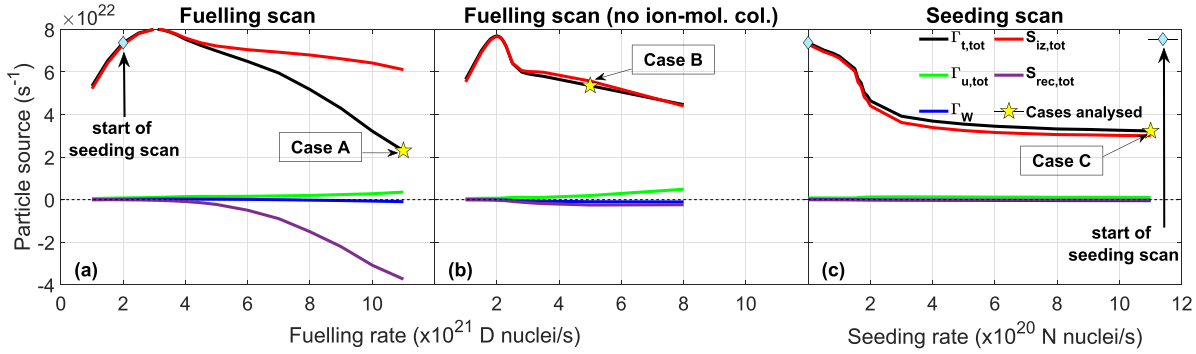

Figure 2. Global particle balance for the yellow region shown in figure 1(*b*) for each scan. The nitrogen seeding scan is carried out at a fixed fuelling rate 2×10^{21} *D* nuclei s^{-1}, marked with diamonds. The cases marked with stars are chosen for further analysis to understand the reason for the differences in recombination levels.

2.2. Role of EIR in target particle flux reduction

An important quantity used in experimental detachment studies is the ion flux incident on the target, the evolution of which is typically used to identify detached divertor conditions. As the electron temperature is continuously reduced (e.g. density ramp, extrinsic impurity scan), the ion target flux rises in the attached (high recycling) regime, and rolls-over and then decreases in the detached phase. We have also used this measure in analysis of the fuelling and seeding scans included in this study. In the following, we will discuss the processes involved in increasing or reducing the plasma flux reaching the divertor in each scan.

Since SOL currents are not included in these simulations, the radially integrated electron and ion fluxes to the target, $\Gamma_{\mathrm{t,tot,e}}$ and $\Gamma_{\mathrm{t,tot,i}}$, are equal: $\Gamma_{\mathrm{t,tot,e}} = \Gamma_{\mathrm{t,tot,i}} = \Gamma_{\mathrm{t,tot}} = \sum_{\mathrm{is}} Z \times \Gamma_{\mathrm{is}}$, where Z is the ionisation state of an ion species is and Γ_{is} is the corresponding ion flux reaching the target. Figure 2 shows the general development of $\Gamma_{\mathrm{t,tot}}$ to the outer lower target in each case, from high-recycling through into their respective detached states. Each of the fuelling scans evidence a rise in $\Gamma_{\mathrm{t,tot}}$ before a drop. A reduction in $\Gamma_{\mathrm{t,tot}}$ can be seen for fuelling rates greater than 3×10^{21} *D* nuclei s^{-1} in figure 2(*a*) and greater than 2×10^{21} *D* nuclei s^{-1} in figure 2(*b*). As mentioned earlier, the seeding scan, figure 2(*c*), is carried out at fuelling rate 2×10^{21} *D* nuclei s^{-1} (light blue diamond in figure 2(*a*)). In contrast to the fuelling scans, only a reduction in $\Gamma_{\mathrm{t,tot}}$ is observed in the seeding scan. This difference between nitrogen seeded and upstream density driven detachment has also been observed in recent TCV experiments [35], where the nitrogen seeding rate was ramped up at two different line-averaged densities.

In order to properly understand which process or processes lead to the target current reduction, we have analysed the various electron sources and sinks integrated over the entire region between the outer lower divertor entrance and the target (highlighted in yellow in figure 1(*b*)). Through particle balance, $\Gamma_{\mathrm{t,tot}}$ is given by equation (1):

$$\Gamma_{\mathrm{t,tot}} = \Gamma_{\mathrm{u,tot}} + S_{\mathrm{iz,tot}} + S_{\mathrm{rec,tot}} + \Gamma_W. \quad (1)$$

Here $S_{\mathrm{iz,tot}}$ and $S_{\mathrm{rec,tot}}$ are the volume integrated electron sources due to ionisation and EIR respectively (when sources are negative they correspond to sinks). Γ_W is the poloidally integrated electron flux lost from the computational domain due to radial transport and $\Gamma_{\mathrm{u,tot}}$ is the total upstream electron flux entering the domain along the flux surfaces. Contributions to $\Gamma_{\mathrm{t,tot}}$ from the RHS terms of equation (1) are also shown in figure 2 for each scan. It can be seen be seen that $\Gamma_{\mathrm{u,tot}}$ and Γ_W are negligible throughout each scan and that $S_{\mathrm{iz,tot}}$ makes the dominant contribution to $\Gamma_{\mathrm{t,tot}}$.

One clear difference between the various scans is the strong contribution from $S_{\mathrm{rec,tot}}$ at high D_2 fuelling rates in the fuelling scan shown in figure 2(*a*), which is always negligible in figures 2(*b*) and (*c*). This difference is a result of lower target temperatures and higher electron densities achieved in the scan corresponding to figure 2(*a*). Importantly, this difference in the temperatures and densities in the fuelling scans is present at similar midplane densities (section 3). As mentioned earlier, the focus of this work is to explain how $D^+ - D_2$ elastic collisions provide access to lower temperatures and higher densities near the target which result in strong EIR conditions in the fuelling scan shown in figure 2(*a*), and the reasons why we see higher target temperatures and lower densities (which result in EIR playing a negligible role) in the seeding scan, as well as when $D^+ - D_2$ elastic collisions are removed from the fuelling scan. To understand this effect better, we take a closer look at an individual case from each scan.

The individual cases for further analysis, cases A, B and C (highlighted with a yellow star in figure 2), are chosen as follows. At any given fuelling or seeding rate, a varying fraction of the power flowing into the divertor from upstream is dissipated between the *X*-point and the divertor target over a poloidally-localised region through a variety of processes. In the rest of this work, for a flux tube, we define the region across which the power dissipated ranges from 5% to 95% of the power entering at the *X*-point position as the 'thermal front' region (section 3.2), as the temperature drops quickly through it due to the removal of power (similar to that in [36, 37]). This region is shown in figures 3(*a*)–(*c*) for each case. In our simulations, for attached plasmas (when $\Gamma_{\mathrm{t,tot}}$ increases for increasing fuelling rate or when the seeding rate is less than 1.5×10^{20} *D* nuclei s^{-1}), the cold end of the thermal front region (in flux tubes close to the separatrix) stays at the target. The roll-over in $\Gamma_{\mathrm{t,tot}}$ in the fuelling cases and the sharp reduction in $\Gamma_{\mathrm{t,tot}}$

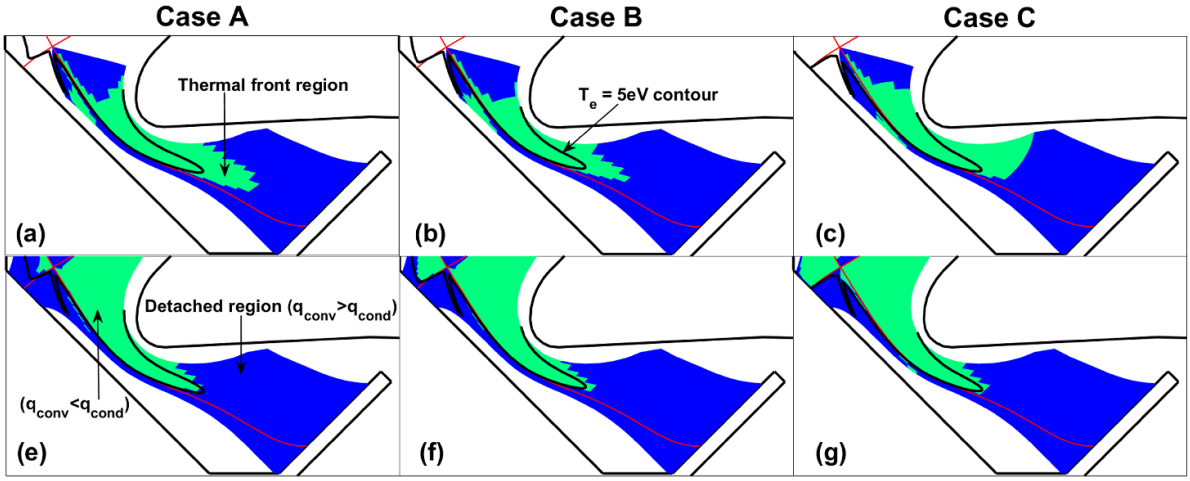

Figure 3. (*a*)–(*c*) The region across which the power dissipated ranges from 5% to 95% of the power entering at the *X*-point position, i.e. the thermal front region. (*d*)–(*f*) Extent of the outer lower detached region in the cases chosen for analysis (marked with stars in figure 2). Regions where parallel heat convection is greater than parallel conduction are marked blue and defined as the 'detached' region in this work. It can be seen that the extent of the detached region is similar amongst the cases chosen for analysis.

in the seeding case occur as the thermal front moves away from the target and towards the *X*-point. Once the thermal front leaves the target, a low temperature region exists between the target and the cold end of the thermal front. The temperature is low enough that heat transport due to conduction is negligible and convection is the dominant heat transport mechanism. In this work, we define the detached region as the region in the divertor across which convection is the dominant parallel heat transport mechanism. The point in the thermal front where the conducted heat becomes equal to the convected heat is defined as the start of the detached region in the rest of this work. Since the seeding scan is performed at a mostly fixed midplane density, we compare cases in which the poloidal extent of the detached region is similar—cases A, B and C. The region in the divertor where parallel heat convection is greater than conduction is shown in figures 3(*d*)–(*f*) for the three cases chosen for further analysis. It can be seen that the spatial extent of the detached region in the poloidal plane is similar for the three cases. As can be seen in figure 3, when the thermal front and detached region are defined in this way, there is some overlap between these two regions. Also shown in figure 3 is the $T_e = 5$ eV contour for each case. It is interesting to see that this roughly coincides with the start of the detached region. In the next section, we analyse these cases in further detail and explore the reasons for the observed differences between the two routes to detachment.

3. Comparison of strongly detached solutions

As demonstrated in the previous section, there are important differences in divertor plasma characteristics between the various paths to detachment when a well-detached state is reached in these simulations. We now take a closer look at cases A, B and C highlighted in figure 2. We focus our analysis on a single flux tube (SOL ring 5), shown in pink in figure 1(*b*). This flux tube, which has been chosen for all 'flux tube' analyses presented here, delivers the peak particle flux to the target when the fuelling rate is 2×10^{21} *D* nuclei s^{-1} (no nitrogen, ion molecule elastic collisions included, blue diamonds in figure 2), i.e. the 'attached' case common to the fuelling scan and the seeding scan. We choose this flux tube for analysis because it is not affected as strongly by radial losses as, for example, the flux tube which delivers the peak heat flux to the target, but is still not too far from the separatrix. Some basic characteristics of the plasma in this flux tube are summarised for each case in table 2.

Table 2. Values of the electron density and temperature at the outboard midplane, $n_{e,u}$ and $T_{e,u}$, and target, $n_{e,t}$ and $T_{e,t}$; parallel heat flux density at the *X*-point position, $q_{||,div}$, and at the start of the detached region, $q_{||,det}$, and the target, $q_{||,t}$; particle flux density at the target, $\Gamma_{||,t}$, and deuterium ionisation potential, $E_{pot} = 13.6$ eV; and plasma pressure at the outboard midplane, $P_{tot,u}$, and the target, $P_{tot,t}$.

	Case A	Case B	Case C
$n_{e,u}$ ($\times 10^{19}$ m^{-3})	1.6	1.5	0.9
$n_{e,t}$ ($\times 10^{19}$ m^{-3})	7.5	4.5	3.5
$T_{e,u}$ (eV)	37.4	41.6	50.7
$T_{e,t}$ (eV)	0.21	0.84	0.84
$q_{||,div}$ ($\times 10^{7}$ Wm^{-2})	2.3	2.7	3.0
$q_{||,det}$ ($\times 10^{6}$ Wm^{-2})	3.6	4.3	1.7
1 - $q_{||,t}/q_{||,div}$	0.99	0.99	0.99
1 - $(q_{||,t} + \Gamma_{||,t}E_{pot})/q_{||,div}$	0.98	0.96	0.98
1 - $P_{tot,t}/P_{tot,u}$	0.95	0.85	0.77

As mentioned earlier, cases A and B have similar outboard midplane densities ($n_{e,u}$) and temperatures ($T_{e,u}$). Case C has a lower $n_{e,u}$ (as expected) and a higher $T_{e,u}$. We note that the parallel heat flux density at the *X*-point position ($q_{||,div}$) is ≈25% lower in case A and 10% lower in case B compared to that in case C. As the density is increased in cases A and B, the midplane profiles in the core region appear to evolve such that the power entering the low field side SOL reduces and the

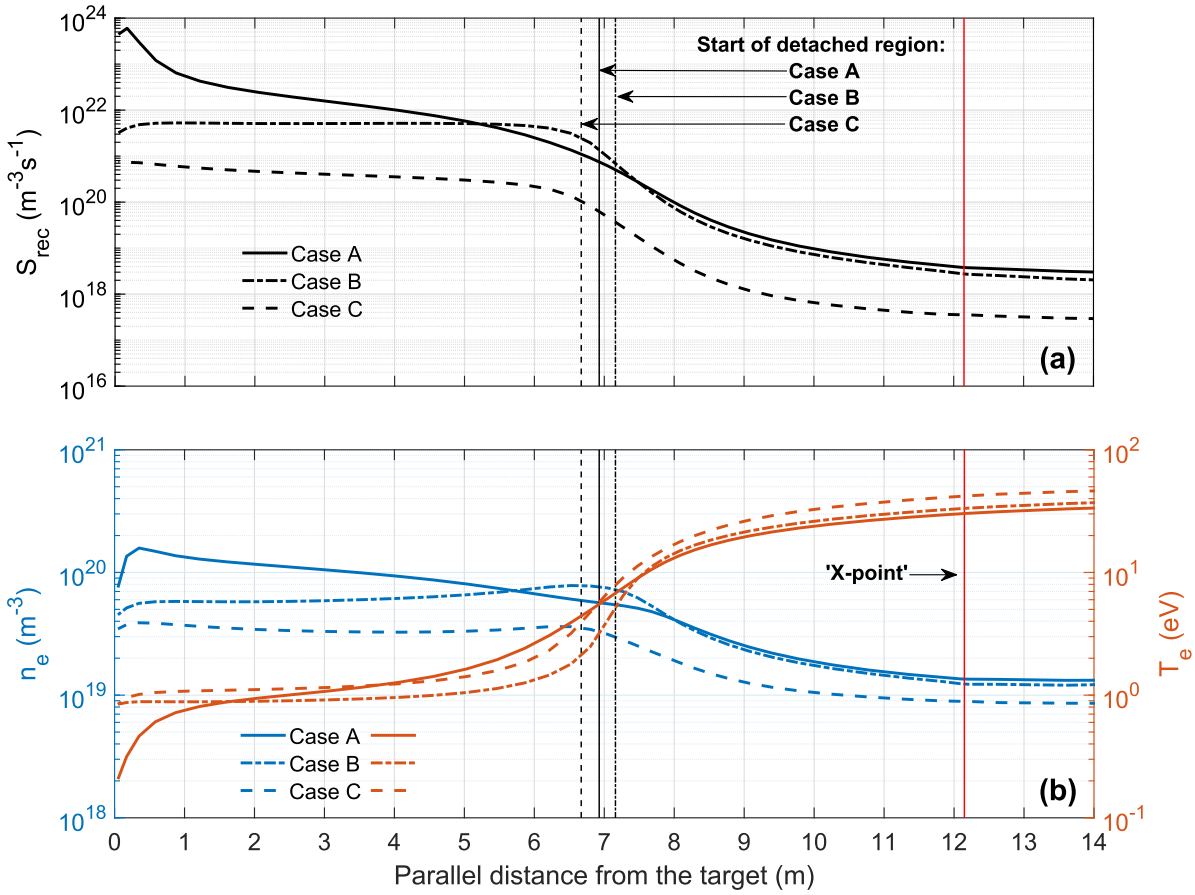

Figure 4. 1D profiles of (*a*) S_{rec} and (*b*) n_e and T_e from cases A, B and C for the flux tube highlighted in pink in figure 1(*b*). The vertical lines at ∼7 m represent the start of the detached region (see figure 3). Higher densities and sub-eV temperatures are achieved in case A leading to high recombination levels.

difference goes into the high field side SOL in these cases. It is not clear at this stage if this redistribution of the input power is physical. However, it seems unlikely that the higher $q_{||,div}$ in cases B and C leads to the negligible recombination levels observed in these cases. This is because parallel heat flux density entering the detached region ($q_{||,det}$) in case C is actually significantly lower than that in cases A and B. In the next and the following subsections, we study the impact of the temperature and density on recombination levels, and discuss the relationship between divertor impurity and neutral levels, and the thermal front characteristics. This is followed by a description of how neutrals and impurities affect the plasma energy, momentum and particle balance across the detached region and shape the corresponding temperature and density profiles.

3.1. Impact of density and temperature on EIR

We will now investigate whether the difference in EIR between the three cases can be explained by temperature differences, electron density differences or both. We utilise figure 4 for this discussion, where the net volumetric recombination sink, S_{rec}, electron density, n_e, and temperature, T_e, profiles along the flux tube are displayed for each case as a function of the parallel distance from the target. The *X*-point position and the start of the detached region are marked with vertical lines.

As pointed out in the discussion of figure 2, S_{rec} is different amongst the three cases. In case C, S_{rec} increases by almost an order of magnitude across the detached region but still is the lowest everywhere in the divertor amongst the three cases. In case B, S_{rec} also increases by almost an order of magnitude but only at the start of the detached region and changes little across most of the detached region. In case A, S_{rec} increases by almost three orders of magnitude between the start of the detached region and the target. The majority of the recombination is localized very close to the divertor plate; there is a sharp increase (by more than an order of magnitude) across the region between 0 m and 1 m parallel distance from the target. These features of S_{rec} are reflected in the T_e and n_e profiles, shown in figure 4(*b*). The thin region of strong recombination in figure 4(*a*) coincides with a similarly thin sub-eV region in figure 4(*b*). We also observe a qualitative difference between the n_e profile in case A and the ones in cases B and C—while there is little change in n_e across the detached region going towards the target in cases B and C, it increases significantly (more than ×2) across the detached region in case A (discussed further in section 3.3).

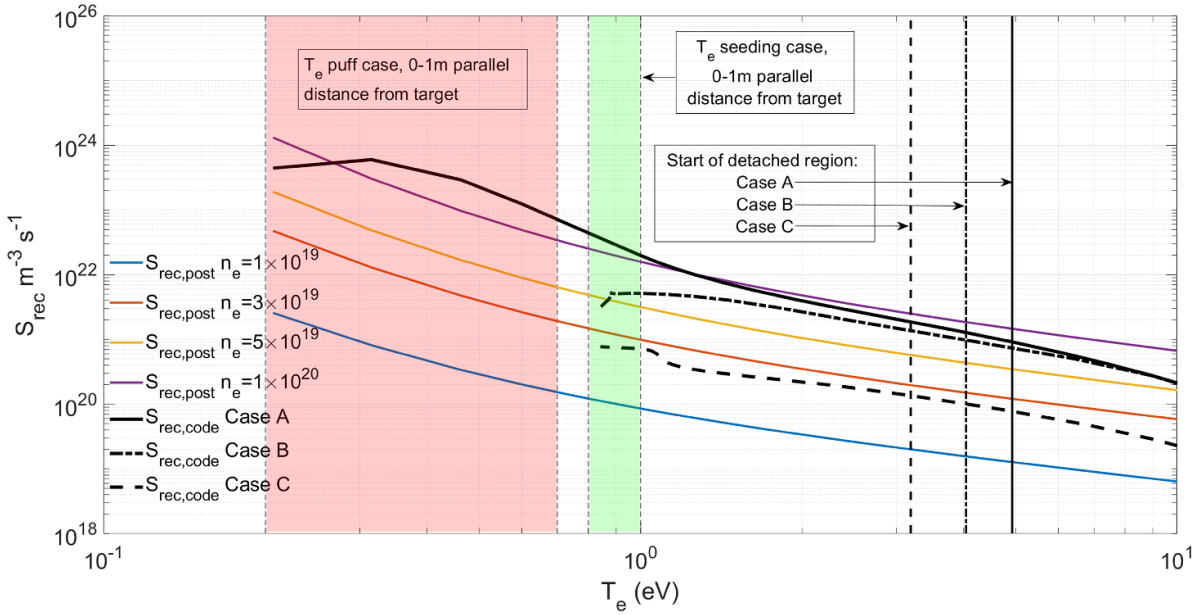

Figure 5. Comparison of the recombination sink post-calculated using AMJUEL at fixed n_e ($S_{rec,post}$) and the recombination sink obtained from the code ($S_{rec,code}$) for each case as a function of T_e. Recombination levels are strongly enhanced at sub-eV temperatures for all densities.

Since the EIR rate depends both on density and temperature, those two plasma characteristics are determining the resultant S_{rec} profiles. The question we address now is which of density and temperature is the dominant determinant of the EIR rate and in which regions. We utilise figure 5 for this discussion where the S_{rec} profiles obtained from the code shown in figure 4(*a*) are re-plotted (and renamed as $S_{rec,code}$) as a function of the corresponding T_e for each case. The temperatures at the start of the detached region are marked with vertical lines. As mentioned earlier, the region of strong recombination for case A is localised between 0 m and 1 m parallel distance from the target for the flux tube considered. The temperature range in this region is highlighted in red for case A and in green for case C (the corresponding T_e range for the case B falls within the green region). To separate the effects of n_e and T_e on the recombination levels, we have used the T_e profile from case A shown in figure 4(*b*) along with rate coefficients obtained from AMJUEL (H.4 2.1.8) to calculate the EIR rate for four fixed densities, $S_{rec,post}$ ($\approx n_e^2 < \sigma v_{rec}(T_e, n_e) >$, for $n_{D^+} \approx n_e$), also displayed in figure 5 as a function of T_e to compare to the $S_{rec,code}$ profiles.

For cases B and C, we find that over the detached region with $T_e \geqslant 1$ eV, the temperature is the dominant factor determining the *rise* of $S_{rec,code}$ in each case as there is little change in density for the individual cases over that temperature region. While this is also true for case A, the increase in n_e does appear to make a considerable contribution. On the other hand, it can be seen that the differences between $S_{rec,code}$ amongst the three cases in the $1\,\text{eV} - 10\,\text{eV}$ region are driven by differences in density. This picture changes when examining the region of $T_e \leqslant 1$ eV, reached only by case A. It can be seen that $S_{rec,post}$ is not as sensitive to temperature in the range $1\,\text{eV} \leqslant T_e \leqslant 10\,\text{eV}$ as compared to when $T_e \leqslant 1\,\text{eV}$. For all four individual densities, $S_{rec,post}$ increases only by roughly an order of magnitude as the temperature drops from 10 eV to 1 eV, and then by about two orders of magnitude as it drops to 0.2 eV. For case A, even though there is a slight drop in density over the low temperature region, $S_{rec,code}$ increases by almost two orders of magnitude indicating that achieving such temperatures is required to reach high levels of EIR.

It will be shown in section 3.3 that the differences in the plasma densities and temperatures amongst the three cases is due to differences in the divertor impurity and neutral levels and their impact on energy, momentum and particle balance across the detached region. This difference in the divertor impurity and neutral levels is related to differences in the thermal front power loss composition upstream of the detached region. Fundamentally, it is this power loss composition that is operationally different in the strongly detached solutions obtained from the fuelling and seeding scans. So in the next subsection, we will discuss the relationship between the various power sinks in the thermal front and the divertor impurity and neutral levels.

3.2. Relationship between thermal front characteristics and divertor impurity/neutral content

As mentioned earlier, the thermal front is a localised region in the divertor where most of the power coming in from upstream is dissipated through various mechanisms. In this work, for a given SOL ring, we define the thermal front as the region across which the total power dissipated along the field due to all possible mechanisms ranges from 5% to 95% of the power entering the flux tube at the *X*-point. In this subsection, we will compare the thermal front characteristics in each of the three cases chosen for analysis and describe how the differences in

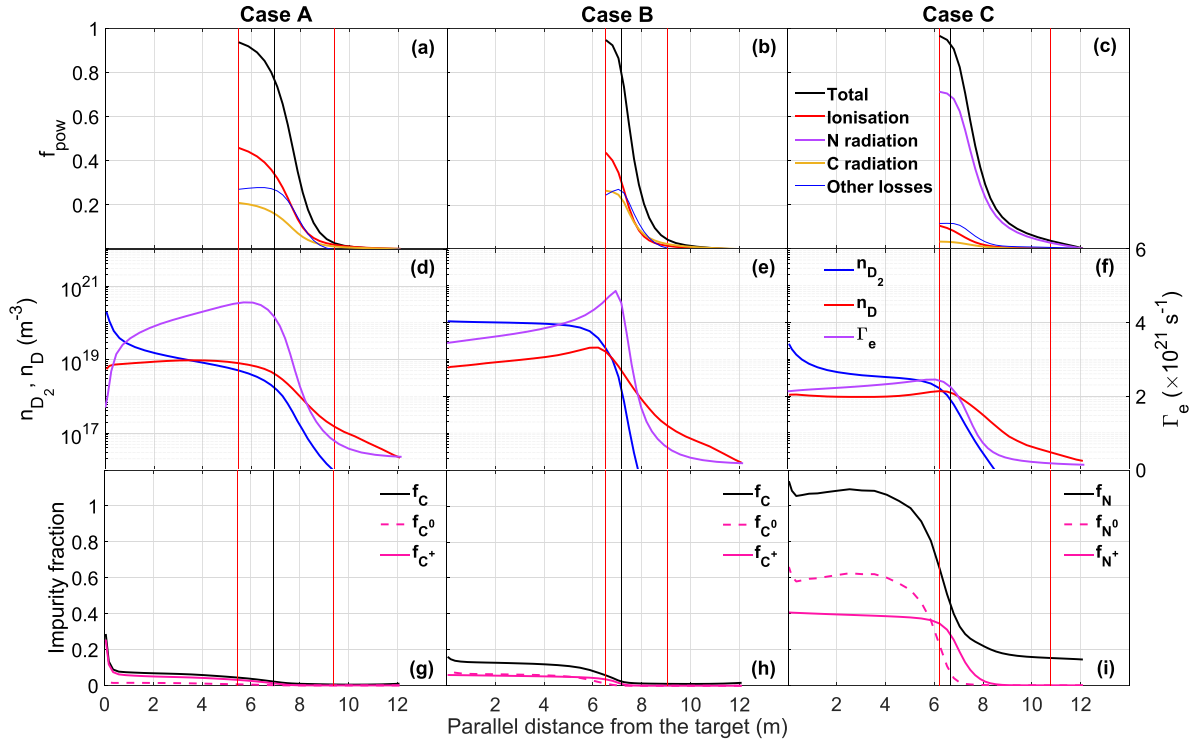

Figure 6. Figures (*a*)–(*c*): the thermal front power loss composition. Since the power entering the divertor in all cases is similar, this means that more plasma is created in the thermal front in cases A and B. Figures (*d*)–(*f*): parallel electron flux Γ_e (right *y*-axis) as a function of parallel distance—plasma flux exiting the thermal front in cases A and B is twice that in C. Figures (*d*)–(*f*): molecular and atomic deuterium densities (left *y*-axis). In the fuelling scans, the neutral densities in the detached region in cases A and B are significantly higher compared to that in case C. Figures (*g*)–(*i*): impurity fraction $f_I = (n_{I^0+\ldots+I^{Z+}})/n_e$, impurity neutral fraction $f_{I^0} = n_{I^0}/n_e$ and singly ionised impurity fraction $f_{I^+} = n_{I^+}/n_e$ where $I = C$ or N. In case C, the divertor impurity levels are significantly higher than that in cases A and B. The red vertical lines represent the hot and cold ends of the thermal front and the black vertical line marks the start of the detached region.

the power loss composition of this region correspond to relatively high neutral levels across the detached region in cases A and B; and relatively high impurity levels across the detached region in case C.

In figures 6(*a*)–(*c*), the total cumulative power loss fraction (f_{pow}) is shown for each case along with the contributions from impurity radiation and hydrogenic losses (deuterium excitation and ionisation) as a function of parallel distance from the target for the region between the *X*-point and the cold end of the thermal front. The vertical red lines represent the hot and cold ends of the thermal front (note that the point where convection takes over from conduction, shown previously in figure 4, lies within this thermal front region). The fundamental difference between the fuelling cases and the seeded case is the fact that in the fuelling case, a large fraction of power (≈50%) is lost to deuterium excitation and ionisation with a smaller fraction (≈20%) lost to impurity (carbon) radiation; whereas in the seeded case, most of the power (≈70%) is lost to impurity (nitrogen) radiation with hydrogenic losses only making a small (≈10%) contribution. Other losses primarily correspond to losses due to radial transport in all cases. Given that the power entering the flux tubes at the *X*-point position is similar in each case, for the fuelling cases this leads to much more power available for ionisation of recycled and/or recombined deuterium, and therefore a significantly larger plasma source in the thermal front. In the seeding case, the power available for ionisation is significantly limited by nitrogen radiation, leading to a smaller divertor plasma source.

In detached conditions, the dominant divertor plasma source is neutral ionisation. In cases B and C, since volume recombination is negligible, the neutral content is linked to the ionisation source through recycling. A relatively small ionisation source in the thermal front corresponds to a lower neutral content in the detached region and vice-versa (this may also be true in case A, but EIR likely also plays a role in increasing the neutral content). This can be seen in figures 6(*d*)–(*f*) which displays the deuterium atomic and molecular densities (left *y*-axis, log scale) as well as the parallel electron flux (right *y*-axis, linear scale), Γ_e, for each case. In case A, a large amount of plasma is created in the thermal front and as a result, the plasma flux exiting the thermal front is twice that in case C. This plasma flows towards the target through a neutral cloud that is about five times as dense as that in case C, leading one to expect significantly higher plasma-neutral interactions across the detached region in case A. This has important consequences for the plasma energy and momentum balance across the detached region.

Just like a large ionisation source in the thermal front means a high neutral density in the detached region, a larger impurity radiation power sink in the thermal front can correspond to higher impurity levels in the detached region. This can be seen in figures 6(*g*)–(*i*) which display the carbon fraction, $f_C = (n_{C^0+\ldots+C^{6+}})/n_e$, from cases A and B and the nitrogen fraction, $f_N = (n_{N^0+\ldots+N^{7+}})/n_e$, from case C as a function of the parallel distance from the target. Across the detached region in cases A and B, it can be seen that $f_C \sim 0.1$ and $f_C \sim 0.15$ respectively. The impurity fraction in case C is significantly higher than that in the non seeded cases. While there is little change in the nitrogen fraction between the divertor entrance ($f_N \sim 0.15$) and about halfway into the thermal front ($f_N \sim 0.2$), it increases significantly across the rest of the thermal front and continues to increase before saturating around 4 m, and stays higher than 1 across the rest of the detached region where the nitrogen radiation density is actually less than 5% of the maximum (note that the impurity fraction can go above 1 when impurity neutrals are included in the definition as we have done here). The localised nitrogen radiation region is sustained by a flow of nitrogen into the thermal front from a relatively dense cloud of nitrogen atoms in the detached region. The average nitrogen fraction in this flux tube, $< f_N >_{\text{average}} = 0.39$, is strongly weighted by the nitrogen (mainly N^0 and N^+) in this low-radiation cloud across a rather large detached region. The large fraction of singly ionised nitrogen, $f_{N^+} = n_{N^+}/n_e$, likely has important consequences for the divertor plasma energy and momentum balance. We note that this impurity fraction may seem high compared to experimentally reported values. However, impurity concentration measurements rely on the emission from higher charge states. So values of f_N reported in experiments typically represent estimates of the concentration in the higher temperature radiating region of the thermal front. Concentration in the cold regions of low radiation is generally not measured, and it is possible that the concentration in these regions is higher than what is reported in experiments. On the other hand, impurity neutralisation is not included in our simulations—studying the impact of including this has not been possible, and the degree to which this would change the nitrogen particle balance is not immediately clear.

As an aside, it is interesting to note the differences in the D_2 density profile between the three cases. In both cases A and C, there is a sharp increase in the molecular density near the target, but this is not observed in case B. As seen earlier, the temperature across the detached region is similar and mostly constant in cases B and C. Further, there is little change in density in both cases—yet the sharp increase in n_{D_2} near the target is present in this case. It is therefore unlikely that differences in dissociation levels is play a significant role in driving the sharp change in the molecular density near the target in cases A and C. This is reflected in the n_D profiles: a corresponding change in n_D in not observed in this region. Ion-molecule elastic collisions are present in cases A and C but not in case B. This seems to suggest that this interaction essentially keeps the molecules 'squashed' near the target. We also note that the hydrogenic power loss in cases A and B is nearly twice that due to carbon radiation. This is in contrast to the TCV simulations presented in [31], where the power loss due to carbon is several times the hygrogenic losses. These TCV simulations use lower main ion recycling fraction (0.99 compared to 1 in these simulations), a higher chemical sputtering yield (3.5% compared to 3% in these simulations) and a lower input power (0.4 MW compared 2.5 MW in these simulations); all of which may lead to this observed difference in the hydrogenic and carbon radiation losses.

To summarise, a thermal front in which hydrogenic losses make the dominant contribution corresponds to a scenario where a relatively large plasma flux exits the thermal front to interact with a relatively high neutral density cloud across the detached region downstream. On the other hand, when the losses are dominated by impurity radiation, this corresponds to a relatively small plasma flux, but with a high impurity fraction, exiting the thermal front and flowing through a relatively low neutral density cloud across the detached region. In the next subsection, we will discuss the consequences of these differences in the neutral and impurity levels on the energy, momentum and particle balance across the detached region and how this relates to the corresponding temperature and density profiles.

3.3. Energy, momentum and particle balance in the detached region

We have seen that the differences in S_{rec} result from differences in the plasma density and temperature profiles. We have also seen that differences in the thermal front power loss composition have a relation to the neutral and impurity levels in the detached region. In this subsection, we will look at how these neutrals and impurities affect the energy, momentum and particle balance across the detached region, and how they shape the corresponding plasma temperature and density profiles in each case. Since the qualitative features of the detached solutions obtained through seeding are recovered in the fuelling scan by turning off $D^+ - D_2$ elastic collisions, we focus our analysis on the impact of this particular interaction on the balances and show how these elastic collisions lead to lower T_e and higher n_e in case A, and discuss how in case C, in addition to lower plasma and molecule densities (and therefore fewer collisions), the N^+ in the detached region may be acting like a reservoir of heat and momentum, resulting in higher T_e near the target and lower n_e across the detached region in this case.

3.3.1. Impact of $D^+ - D_2$ elastic collisions on energy and momentum balance across the detached region. Since the focus of this section is to describe the impact of $D^+ - D_2$ interactions, we only consider the ion energy balance, which does not directly involve T_e. However, across most of the detached region, we find that the ion and electron temperatures are roughly equal ($0.98 < T_i/T_e < 1.02$ between 0 and 4 m from the target, $T_i/T_e \approx 2$–3 at the outboard midplane in this SOL ring) and therefore strongly coupled in each case—a drop in T_i corresponds to a similar drop in T_e. We also find that ion heat conduction ($q_{||,i,\text{cond}}$, shown in figure 7(*a*)–(*c*)) is

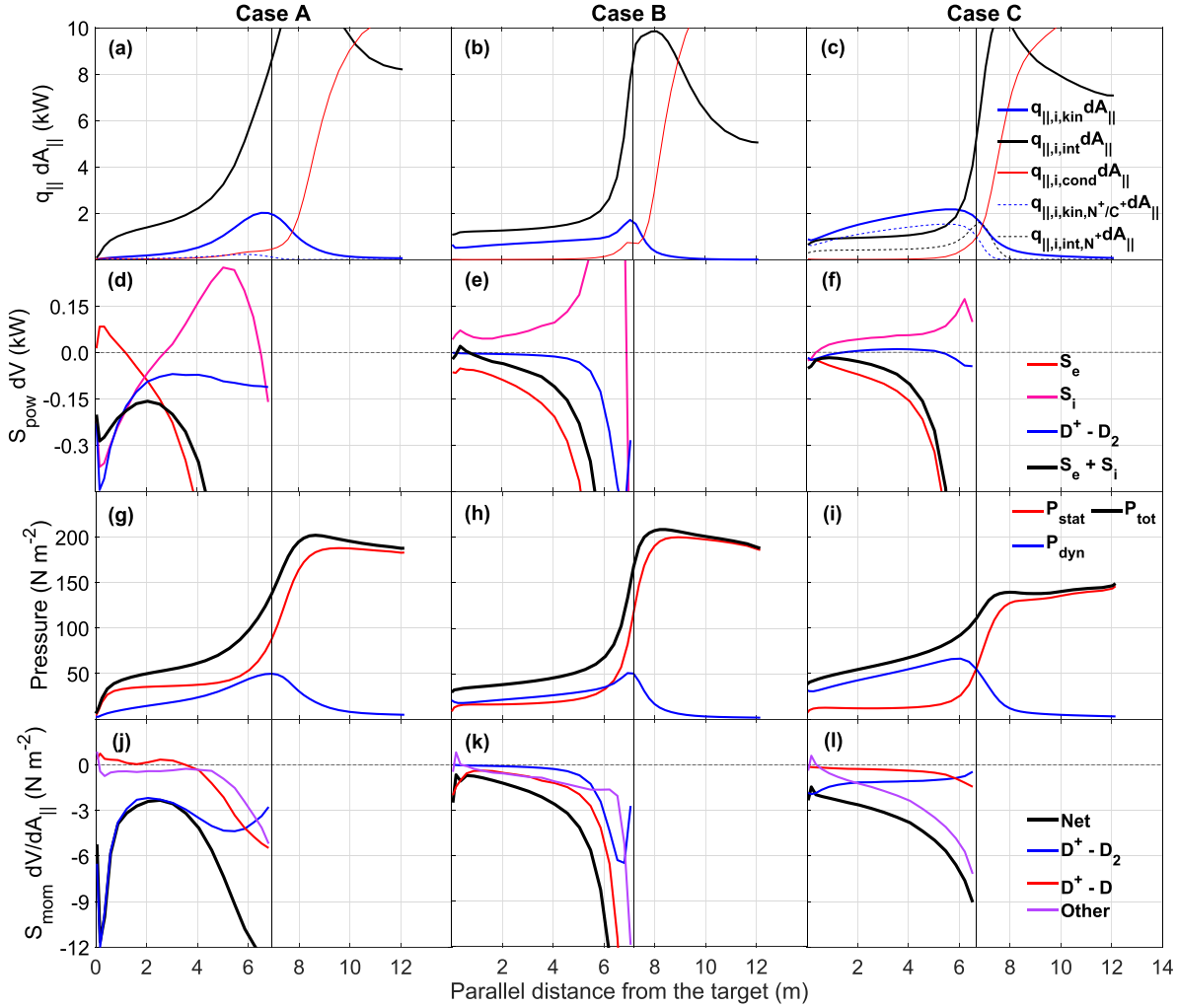

Figure 7. The impact of $D^+ - D_2$ interactions on the RHS terms of equation (2), $q_{||,i,kin}$ and $q_{||,i,int}$, is summarised through a power and momentum balance analysis. $q_{||,i,kin}$ and $q_{||,i,int}$ are shown in (*a*)–(*c*), along with $q_{||,i,cond}$, $q_{||,i,int,N^+}$ (internal energy associated with N^+) and the directed kinetic energy associated with C^+ for case A and N^+ for case C, $q_{||,i,kin,N^+/C^+}$. Most of $q_{||,i,kin}$ in case C is composed of $q_{||,i,kin,N^+}$, and $q_{||,i,int,N^+}$ makes up for a significant fraction of $q_{||,i,int}$. Figures (*d*)–(*f*) show the power loss/gain through the ion and electron channels, S_i and S_e, the net power exchange, $S_i + S_e$ and power exchange through $D^+ - D_2$ interactions. The changes in $S_i + S_e$ result in corresponding changes in $q_{||,i,int}$ (and therefore in temperature). Figures (*g*)–(*i*) show profiles of P_{tot}, P_{stat} and P_{dyn}. Figures (*j*)–(*l*) provide information on the mechanisms that lead to changes in P_{dyn} and therefore $q_{||,i,kin}$.

small compared to convection ($q_{||,i,conv}$) across the detached region in all cases, and therefore do not include it in our energy balance analysis. Ignoring viscous effects, the total convected ion energy ($q_{||,i,conv}$) flowing along a fluxtube of cross-sectional area $A_{||}$ is given by equation (2), where $q_{||,i,kin}$ and $q_{||,i,int}$ are the directed kinetic energy density and the internal energy density components of $q_{||,i,conv}$ (also displayed in figures 7(*a*)–(*c*)); and m_{is}, n_{is} and $v_{is,||}$ are the mass, density and the velocity component parallel to B of an ion species is, which we use to calculate $q_{||,i,int}$ and $q_{||,i,kin}$,

$$q_{||,i,conv} = q_{||,i,kin} + q_{||,i,int,} = \sum_{is} \frac{m_{is} n_{is} v_{is,||}^3}{2} + \frac{5eT_i}{2} \sum_{is} n_{is} v_{is,||}. \quad (2)$$

Changes in T_e described earlier are correlated with changes in $q_{||,i,int}$ rather than $q_{||,i,kin}$. As can be seen in figure 4(*b*), T_e in each case starts to saturate as it drops from a few eV at the start of the detached region and approaches ≈1 eV. The main difference is that while T_e saturates at ≈1 eV in cases B and C, in case A it undergoes another significant reduction between the target and ∼2 m from the target, dropping to ∼0.2 eV. This is correlated with how $q_{||,i,int}$ changes as a function of parallel distance in each case, shown in figures 7(*a*)–(*c*): in case A, between $0 - 2$ m from the target, $q_{||,i,int}$ undergoes a second significant reduction, falling to values that are roughly 10 and 15 times smaller than that in cases B and C.

The reduction in $q_{||,i,int}$ between 0 m and 2 m in case A is driven by enhanced heat transfer to molecules through $D^+ - D_2$ interactions, which only make a small net

contribution to the internal energy balance across the detached region in case C—this results in lower temperatures near the target in case A compared to case C. Changes in $q_{||,i,int}$ are a result of the various sources and sinks of internal energy—profiles of the net internal energy loss through the electron and ion channels, S_e and S_i, and the net internal energy sink, $S_e + S_i$, are shown in figures 7(*d*)–(*f*). It should be noted here that (*a*) since S_e and S_i are internal energy sinks, they directly affect $q_{||,i,int}$ but not $q_{||,i,kin}$; and (*b*), the fact that we have not included currents in these simulations and that $T_i \approx T_e$ implies that $q_{||,i,int} \approx q_{||,e,int}$ and that S_e also results in a drop in $q_{||,i,int}$. In fact, losses due to S_e are dominant at the start of the detached region in all cases, but weaken significantly going towards the target as the temperature approaches 1 eV. The drop in $q_{||,i,int}$ near the target in case A is driven by a relatively strong net internal energy sink compared to that in case C. The difference between the net internal energy sink profiles of cases A and C is due to differences in S_i. In case C, S_i weakly heats the plasma across most of the detached region, but in case A it changes sign at ≈3 m and becomes an increasingly strong power sink as we move towards the target. In case A, S_i drives the net power loss between 0 m and 2 m (and therefore the reduction in $q_{||,i,int}$ and temperature). S_i is mainly due to interactions between D^+ and D atoms, D^+ and D_2 molecules and also D_2^+ and electrons (if a D^+ ion is created as a result). The contribution to S_i from $D^+ - D_2$ interactions is also shown in figures 7(*d*)–(*f*) for each case. It can be seen that the strong losses between 0 m and 2 m in case A are driven by $D^+ - D_2$ interactions; whereas in case C, these interactions only make a small contribution to the internal energy balance.

In cases A and C, $D^+ - D_2$ interactions consist of ion-molecule elastic collisions and ion-conversion, but current code diagnostics do not allow us to directly distinguish between these two interactions. As mentioned earlier, ion-molecule elastic collisions are excluded in case B and only ion-conversion is retained. It can be seen that in this case, the $D^+ - D_2$ trace makes a contribution to S_i only at the start of the detached region—across most of the detached region, the $D^+ - D_2$ trace makes a negligible contribution to the power balance. Power loss in general is weak between 0 m and 4 m from the target and consistent with the relatively constant $T_e \approx 1$ eV in this region. For the default ion-conversion cross-sections used by SOLPS-ITER (and hence in these simulations), this suggests that ion-conversion is only active at relatively high temperatures ($T_e \geqslant 1$ eV) and likely makes a negligible contribution to S_i between 0 m and 2 m in cases A and C. It also suggests that the drop in $q_{||,i,int}$ in this region in case A is driven mainly by ion-molecule elastic collisions. In case C, $D^+ - D_2$ interactions are a weak power sink at the start of the detached region where the temperature is relatively high—therefore this is likely due to ion-conversion; however between 2 m and 5 m, $D^+ - D_2$ interactions weakly heat the plasma. Ion-conversion is a D^+ sink, so this interaction should also remove the associated energy—therefore ion-conversion cannot heat the plasma. This means that it is the ion-molecule elastic collisions that are weakly heating the plasma in this region. In general, they only make a small contribution to the internal energy balance in case C. We thus conclude that increased internal energy losses due to ion-molecule elastic collisions lead to the significant power loss observed between 0 m and 2 m in case A, providing access to sub-eV temperatures and enhance EIR levels; and that ion-molecule elastic collisions only weakly affect $q_{||,i,int}$ in case C, resulting in a higher T_e and low EIR levels.

At this stage, it is important to emphasise the following. Given the documented discussion in literature about ion-conversion [25, 27, 28, 38], the default ion-conversion cross-sections used by SOLPS-ITER may need to be updated. Ion-conversion cross sections are underestimated in detached conditions, particularly for deuterium. By default, EIRENE performs ion isotope mass rescaling of this rate, $< \sigma v >_{D(T)} = < \sigma v >_{H(T/2)}$. As $< \sigma v >_{H(T)}$ decays strongly at $T < 1$ eV, this leads to a strongly underestimated rate at detachment-relevant conditions for deuterium [28]. Non self-consistent post-processing of these simulations has been performed for diagnostic purposes in [25], which showed that this does not play a significant role in the seeded simulations, but plays a significant role in the density ramp cases after the detachment onset; resulting in significant levels of MAR, hydrogenic emission and MAD—leading to plasma energy losses and additional neutral atoms. This post-processing, which is not self-consistent, is expected to exaggerate the molecular effects by roughly ×2 [28]. It is possible that repeating this study with updated ion-conversion cross-sections may change the solutions discussed in this work such that ion-conversion plays a more significant role. In this work, we can only discuss solutions obtained using the existing ion-conversion cross-sections.

So far, we have only discussed the impact of ion-molecule elastic collisions on $q_{||,i,int}$. In the following, we will discuss their role in $q_{||,i,kin}$ dissipation. In cases A and C, different degrees of $q_{||,i,kin}$ dissipation are observed across the detached region. In case A, most of the $q_{||,i,kin}$ (>95%) is dissipated across the detached region and in case C, around half of the $q_{||,i,kin}$ is dissipated in the same region. The internal energy balance analysis involving figures 7(*a*)–(*f*) only gives us information on how $q_{||,i,int}$ is dissipated but not $q_{||,i,kin}$. Since $q_{||,i,kin}$ is effectively the product of the plasma dynamic pressure and the parallel flow velocity, information on how $q_{||,i,kin}$ is dissipated in both cases can be obtained from a pressure balance analysis.

In figures 7(*g*)–(*i*), the total, static and dynamic pressure profiles (P_{tot}, P_{stat} and P_{dyn} respectively) are shown for each case as a function of the parallel distance from the target. Note that in all cases, there is little change in P_{stat} through most of the detached region and that the reduction in P_{tot} is largely due to P_{dyn}. Figures 7(j)–(l) show the net momentum sink, the contributions from $D^+ - D_2$ and $D^+ - D$ interactions, and the net contribution from all other mechanisms (mostly composed of losses associated with total magnetic flux expansion and radial transport). It can be seen that $D^+ - D_2$ interactions are the dominant momentum sink across most of the detached region in case A and between 0 m and 2 m in case C. This is in contrast to what is observed in the TCV simulations presented in [31], where $D^+ - D$ interactions remove more momentum compared to $D^+ - D_2$ interactions. The exact reason for this

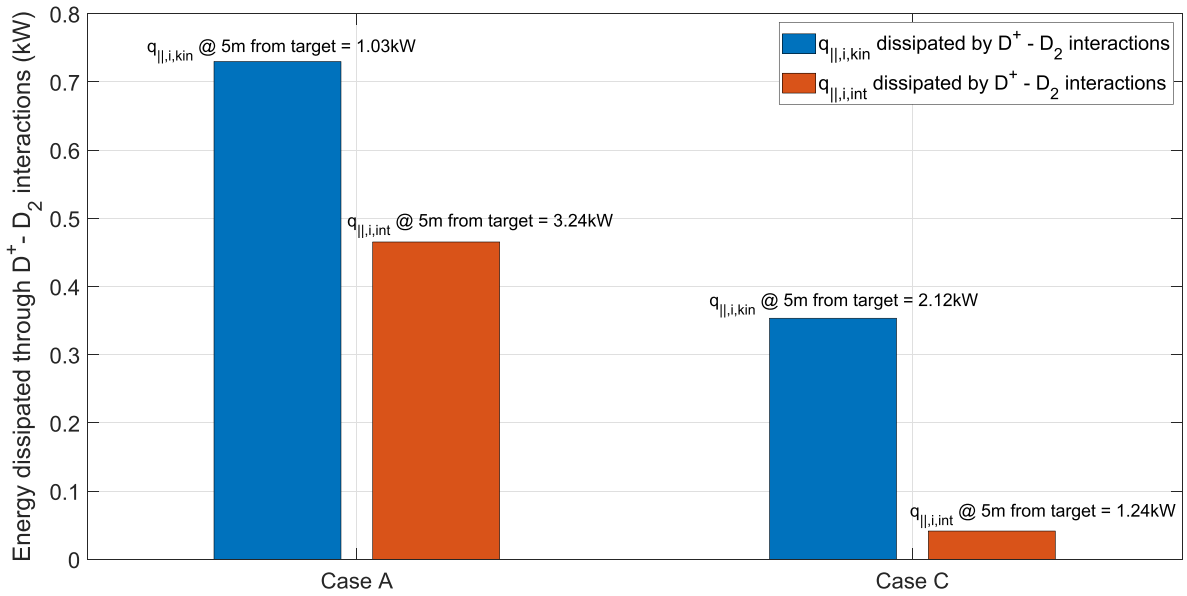

Figure 8. Comparison of $q_{||,i,kin}$ dissipated by $D^+ - D_2$ interactions (calculated using equation (A.2)) and $q_{||,i,int}$ dissipated by the same between 2 m − 5 m for case A and 0 m − 5 m for case C. For both cases, $q_{||,i,kin}$ and $q_{||,i,int}$ at 5 m from the target (amount available to dissipate across the region considered) is indicated. It can be seen that $q_{||,i,int}$ dissipated by this interaction relative to the $q_{||,i,kin}$ dissipated by the same is significantly lower in case C as compared to case A.

difference is not clear, but may be due to different detachment levels. In case A, losses to $D^+ - D$ interactions and other losses (which are the dominant momentum sink at the start of the detached region) weaken significantly across the detached region; and make a negligible contribution between 0 m and 4 m. In case C, while combined losses associated with total flux expansion and radial transport dominate over $D^+ - D_2$ interactions between 2 m and 6 m, the contribution from $D^+ - D_2$ interactions is significant nonetheless (and in fact dominant across most of the detached region if compared to radial and total magnetic flux expansion losses individually). In other words, while $D^+ - D_2$ interactions have a weaker impact on $q_{||,i,int}$ in case C as compared to that in case A, they seem to play an important role in dissipating P_{dyn}, and therefore $q_{||,i,kin}$, in both cases A and C. This indicates that the impact of ion-molecule elastic collisions on $q_{||,i,int}$ relative to that on $q_{||,i,kin}$ may be lower in case C, as compared to that in case A.

The relative impact of $D^+ - D_2$ interactions on $q_{||,i,kin}$ vs. $q_{||,i,int}$ can be quantified by calculating the $q_{||,i,kin}$ dissipated by them: since the net momentum loss, momentum loss due to $D^+ - D_2$ interactions and the total change in $q_{||,i,kin}$ are known, and given that $q_{||,i,kin}$ and P_{dyn} are closely related, the amount of $q_{||,i,kin}$ dissipated by $D^+ - D_2$ interactions can be calculated (appendix 'Role of $D^+ - D_2$ interactions in $q_{||,i,kin}$ dissipation') in regions where P_{stat} is mostly constant (this is because the momentum sinks shown do not necessarily always correspond to P_{dyn} dissipation). We consider the region between ≈2 m − 5 m in case A and ≈0 m − 5 m in case C, where there is little (10%–20%) change in P_{stat}. The $q_{||,i,kin}$ dissipated by $D^+ - D_2$ interactions in cases A and C integrated across the regions considered is shown in figure 8. This is compared with the corresponding $q_{||,i,int}$ dissipated through $D^+ - D_2$ interactions. It can be seen that relative to $q_{||,i,kin}$ dissipation, $q_{||,i,int}$ dissipated by ion-molecule interactions is significantly lower in case C. The ratio of $q_{||,i,int}$ dissipated to $q_{||,i,kin}$ dissipated by this interaction across the regions considered is ≈0.64 in case A whereas in case C it is ≈0.12. It is interesting to note that this is partly because ion-molecule elastic collisions actually (weakly) *heat* the plasma between 2 m and 5 m (in contrast to what is observed in case A), while playing an important role in $q_{||,i,kin}$ dissipation in this case.

The ion internal energy balance analysis has shown that the impact of ion-molecule elastic collisions on $q_{||,i,int}$ is significantly weaker in C as compared to that in case A. The natural question following the internal energy balance analysis is why the impact of ion-molecule elastic collisions on $q_{||,i,int}$ is significantly weaker in case C as compared to that in case A (leading to a higher T_e near the target in case C as compared to that in case A). In general, given the fact that the plasma and molecule densities are lower in case C (and therefore there will be fewer ion-molecule interactions), this is expected. However, while lower plasma and molecule density in the detached region in case C is likely an important part of the reason why ion-molecule elastic collisions only weakly affect $q_{||,i,int}$, this does not explain why their impact on $q_{||,i,int}$ relative to that on $q_{||,i,kin}$ is significantly lower in case C, as compared to that in case A (or why they heat the plasma in case C, albeit rather weakly). This suggests that there could be more reasons why the impact of ion-molecule elastic collisions on $q_{||,i,int}$ is especially weak in case C.

Exactly how the split between $q_{||,i,int}$ and $q_{||,i,kin}$ dissipated through each ion-molecule interaction is calculated is not clear, however, there appears to be a general preference to dissipate $q_{||,i,kin}$ as opposed to $q_{||,i,int}$. Consider case A.

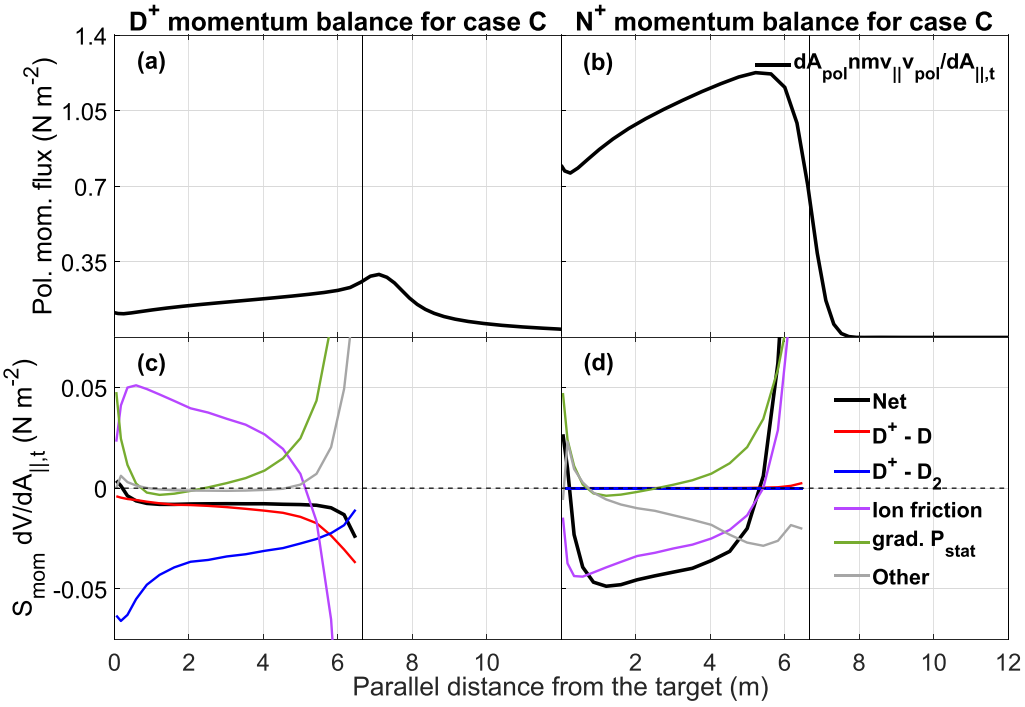

Figure 9. Momentum balance analysis of D^+ and N^+ in case C - (*a*) and (*b*) show the poloidal momentum flux density associated with each species, and (*c*) and (*d*) show a decomposition of momentum sinks. $D^+ - D_2$ interactions are the dominant D^+ momentum sink but a lot of the lost momentum is regained through ion-friction. Ion friction makes a roughly equal and opposite contribution to the N^+ momentum balance, where it is the dominant momentum sink.

Between 2 m and 5 m, the amount of $q_{||,i,int}$ available to dissipate (indicated in figure 8 as $q_{||,i,int}$ @ 5 m from target) is significantly higher (more than $\times 3$) than the amount of $q_{||,i,kin}$ available to dissipate, yet the amount of $q_{||,i,kin}$ dissipated in this region by $D^+ - D_2$ interactions is significantly higher than the $q_{||,i,int}$ dissipated. In fact, most of the $q_{||,i,kin}$ available to dissipate is dissipated between 2 m and 5 m in case A, and between 0 m and 2 m, since there is little $q_{||,i,kin}$ left to dissipate, ion-molecule elastic collisions mainly dissipate $q_{||,i,int}$. If there is indeed a general preference to dissipate $q_{||,i,kin}$, then in addition to the lower plasma and molecule density across the detached region in case C, it is possible that such a preference to dissipate $q_{||,i,kin}$ may also be contributing to the observed weak impact of ion-molecule elastic collisions on $q_{||,i,int}$ since $q_{||,i,kin} > q_{||,i,int}$ at the start and across most of the detached region in this case.

Note that in case C, a large fraction of the plasma in the detached region is composed of nitrogen ions, $f_{N^+} \approx 0.4$ (figure 6). Since nitrogen is seven times heavier than deuterium, most of the kinetic energy is actually carried by N^+, as can be seen in figure 7(*c*) in which the $q_{||,i,kin}$ carried by N^+ alone is also displayed. In fact, this is the reason why $q_{||,i,kin} > q_{||,i,int}$ across most of the detached region in case C. However, N^+ does not interact directly with the molecules in our model. In the next part of this discussion, we will show how the N^+ part of the plasma across the detached region in case C loses energy even though it does not directly interact with the molecules; and more generally, discuss the impact of a large f_{N^+} across the detached region on the plasma solution.

3.3.2. Impact of a large f_{N^+} on the energy and momentum balance. As mentioned above, the N^+ part of the plasma fluid does not interact with any neutrals in our model. In this part of the discussion, through an individual momentum balance analysis of D^+ and N^+, we will show that the nitrogen ions lose energy and momentum via friction with the D^+ fluid which does interact with the neutrals. Even though the nitrogen does not directly interact with the neutrals, the plasma fluid in the detached region loses energy/momentum as a whole through a $D_2 - D^+ - N^+$ interaction chain.

The poloidal momentum flux density associated with D^+ and N^+ is shown for case C as a function of the parallel distance from the target in figures 9(*a*) and (*b*) respectively and the corresponding momentum source decomposition across the detached region is shown in figures 9(*c*) and (*d*). The vertical line marks the start of the detached region. It can be seen that most of the momentum is actually carried by N^+ and not D^+, consistent with the observation in figure 7(*c*). The N^+ fluid is created in the downstream half of the thermal front where a steep static pressure gradient exists, so it undergoes a strong acceleration towards the target as soon as it is created across the interface between the thermal front and the detached region. In the momentum balance for N^+, the momentum loss is primarily driven by ion friction; other losses (mainly radial transport) weaken significantly as the D^+ and N^+ fluids move towards the target. Since most of the plasma in this region is composed of D^+ and N^+ (figure 6), the momentum exchange associated with ion friction is primarily through $D^+ - N^+$ friction. In the D^+ momentum balance, across most of the detached region, the contributions from $D^+ - D$ interactions,

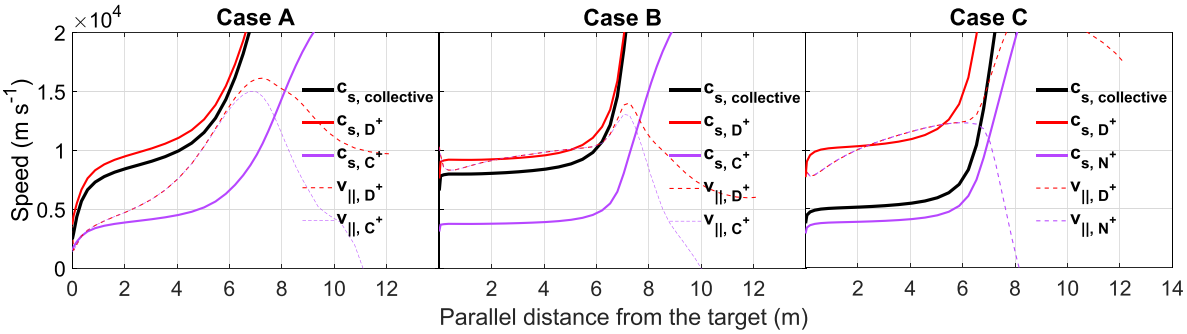

Figure 10. Sound speed profiles of D^+ and the most abundant impurity species in the divertor for each case compared to their corresponding parallel flow velocities. These are also compared to the collective sound speed for all species.

static pressure gradient and the net contribution from all other losses are small. The net momentum sink for D^+ is primarily a balance between losses due to D_2 interactions and momentum gain due to ion friction—while there is a relatively large momentum sink associated with $D^+ - D_2$ interactions, a lot of this 'lost' D^+ momentum is actually regained through friction with N^+. This results in a relatively small net momentum sink and only a small drop in the D^+ poloidal momentum flux is observed. Note that the momentum exchange associated with ion friction in figure 9(*d*) is roughly equal and opposite in figure 9(*c*)—roughly the same amount of momentum is gained by D^+ through ion friction as is lost from N^+. This shows that in case C, while molecules do not act directly on a large fraction of the plasma, the momentum from the whole plasma fluid across the detached region is lost through a $D_2 - D^+ - N^+$ interaction chain.

Just as the strongly accelerated N^+ acts like a reservoir of momentum for the D^+, it is likely that a similar effect is playing a role when it comes to the internal energy. As can be seen in figure 7, the internal energy associated with N^+, $q_{||,i,int,N^+}$, is a significant fraction of $q_{||,i,int}$ in case C. In these simulations, the ion temperature is equal for all ion species. As with the momentum balance, since N^+ does not directly interact with the molecules, the N^+ fluid loses heat mostly via frictional interaction with the D^+ fluid (radiative losses are small due to the low temperature). Thus, the N^+ fluid may be weakening the impact of ion-molecule elastic collisions on $q_{||,i,int}$ by effectively acting like a reservoir of heat or temperature. Another consequence of the fact that a large amount of N^+ is created in the cold end of the thermal front and strongly accelerated by the steep static pressure gradient into the detached region is that at some point, because of the nitrogen mass, we find that $P_{dyn} > P_{stat}$ (figure 7(*i*)). In other words, the plasma goes supersonic as it enters the detached region in case C: in contrast to case A, the neutrals in the detached region in case C interact with a plasma that is actually more comparable to an 'ion beam'. The potential implications of this on how ion-molecule elastic collisions affect the solution in this case will be discussed further in the next part of this discussion.

As an aside, it is useful at this stage to discuss an interesting and important aspect of the solutions presented in this paper. In the absence of drifts, SOLPS by default provides two options for the momentum boundary condition at the sheath. One option is to impose $v_{||,is} \geqslant c_{s,is}$, where $v_{||,is}$ is the parallel flow velocity of species is and $c_{s,is}$ is the corresponding sound speed. This is the option we have chosen in our simulations. Since T_i is the same for all ion species in our simulations, this means that the minimum value of $v_{||,is}$ imposed at the sheath is necessarily different for ion species of different mass. However, as discussed earlier, while the N^+ fluid does not interact with D_2, it 'feels' their presence through frictional interaction with the D^+ fluid. The steady solution is consistent with the plasma fluid as a whole losing momentum through the $D_2 - D^+ - N^+$ interaction chain, with ion friction distributing the momentum loss across the plasma fluid such that the $v_{||,is}$ of all ion species is approximately (but not exactly) equal across the detached region. So as a result, while the chosen boundary condition implies $v_{||,is} \geqslant c_{s,is}$ at the sheath, the ion friction appears to result in *all* plasma species satisfying the minimum $v_{||,is}$ condition on the lightest component of the fluid (because this will have the highest sound speed). This can be seen in figure 10 which shows the parallel flow velocity profiles of D^+ and the most abundant impurity ion species in the detached region in each case, as well as the corresponding sound speed profiles. For the solutions in case C, the mass difference between deuterium and nitrogen implies that a significantly different minimum value of $v_{||,is}$ is imposed on almost half the plasma at the sheath since $f_{N^+} \approx 0.4$ here. Since f_{C^+} across the detached region is relatively small in cases A and B, the chosen target boundary conditions are likely to be reasonable in these cases. However, due to the large f_{N^+} in case C, further work is needed to assess whether this is appropriate for this case.

The second available option for the momentum boundary condition at the sheath (which we have not used) is to set the $v_{||}$ for *all* species to be *equal* to the local *collective* sound speed, $c_{s,\text{collective}}$, which is defined as:

$$c_{s,\text{collective}} \equiv \sqrt{\frac{n_e e T_e + \sum_{is} n_{is} e T_i}{\sum_{is} m_{is} n_{is}}}. \tag{3}$$

The combined effect of the nitrogen mass and a large f_{N^+} is a significantly lower $c_{s,\text{collective}}$. This can be seen in figure 10 which also displays the $c_{s,\text{collective}}$ profile for each case. It can be seen that even though carbon is a lot heavier than deuterium, $c_{s,\text{collective}} \approx c_{s,D^+}$ in cases A and B due to a relatively

small f_{C^+}; and due to a large f_{N^+} in case C, it can be seen that $c_{s,\text{collective}} \approx c_{s,N^+}$. This suggests that using this second option as the momentum boundary condition at the sheath could considerably change the solution in case C.

3.3.3. Summary and discussion of the energy and momentum balance analysis. We have seen from the internal energy balance analysis that the impact of ion-molecule elastic collisions on $q_{||,\text{i,int}}$ is generally weak across the detached region in case C (figure 7). As mentioned earlier, this is generally expected due to the lower plasma and molecule density across the detached region in this case. However, as demonstrated through the pressure balance analysis (figure 8), we found that the impact of the elastic collisions on $q_{||,\text{i,kin}}$ is actually not as weak, suggesting that there could be other mechanisms that result in the rather weak impact on $q_{||,\text{i,int}}$ and thus leading to a higher T_e in case C. We identified two possible reasons why the impact of $D^+ - D_2$ elastic collisions on $q_{||,\text{i,int}}$ is especially weak in case C. We also noted that there appears to be a general preference for the elastic collisions to dissipate $q_{||,\text{i,kin}}$ rather than $q_{||,\text{i,int}}$; and since $q_{||,\text{i,kin}} > q_{||,\text{i,int}}$ across the detached region in case C, we identified this preference as a potential reason for the rather weak impact of the elastic collisions on $q_{||,\text{i,int}}$ in this case. Next, we saw that the high $q_{||,\text{i,kin}}$ in case C is a consequence of the large f_{N^+} across the detached region, and that the multifluid plasma as a whole loses momentum (and therefore $q_{||,\text{i,kin}}$) through a $D_2 - D^+ - N^+$ interaction chain (figure 9). We also noted that since the ion temperature is the same for all the species, the N^+ likely acts like a reservoir of heat or temperature, effectively weakening the impact of the elastic collisions on $q_{||,\text{i,int}}$ in yet another way. Lastly, we noted that another consequence of the large f_{N^+} in case C is that the plasma goes supersonic as it enters the detached region, and that the molecules essentially interact with a 'plasma beam' in this case (figure 10).

Exactly how the energy exchange in an ion-molecule elastic collision is split between $q_{||,\text{i,int}}$ and $q_{||,\text{i,kin}}$ remains unclear—in particular, (*a*) why there appears to be a general preference to dissipate $q_{||,\text{i,kin}}$ rather than $q_{||,\text{i,int}}$ and (*b*) why the elastic collisions in case C heat the plasma in some places and cool it in other places remain unanswered questions. The energy and momentum exchange associated with each ion-molecule elastic collision is calculated as follows: The pre-collision position and velocity vectors of D_2 are known, and the corresponding velocity vectors of D^+ are obtained by sampling the associated drifting Maxwellian distribution at that position. A simple 'billiard ball' collision is then simulated and the post-collision velocities are obtained through energy and momentum balance. For the D^+, the post-collision velocity will have a new parallel-to-B component, $v_{||,D^+}$, that will be associated with a change in $q_{||,\text{i,kin}}$; and also a new 'random' thermal component, v_{th,D^+}. The difference between the pre-collision and post-collision v_{th,D^+} will be associated with changes in temperature/internal energy.

The basic picture in the detached region in these simulations is as follows: a fast flowing plasma (mostly D^+ in case A and a significant f_{N^+} in case C) interacts with a relatively stationary D_2 cloud through elastic collisions (and also ion friction in case C). In such a scenario, it is plausible that the change in $v_{||,D^+}$ is proportional to $v_{||,D^+}$ itself. In other words, the faster the plasma flows through the D_2 cloud, the larger the drag it experiences. This could potentially explain the apparent preference to dissipate $q_{||,\text{i,kin}}$ as opposed to $q_{||,\text{i,int}}$.

The impact of elastic collisions on internal energy would depend on the difference between the pre-collision and post-collision 'random' velocity component of D^+—if the post-collision v_{th,D^+} is larger than the corresponding pre-collision value, then this would represent a source of heat because an increase in v_{th,D^+} means an increase in temperature. This could occur in scenarios where $v_{||,D^+} > c_{s,D^+}$—where the plasma is more like a beam of ions. As mentioned earlier, this is the situation in case C—the relatively stationary D_2 cloud essentially interacts with a 'beam' of plasma. In such a scenario, it is plausible that such an interaction would lead to the 'thermalisation' of the 'beam' - making ion-molecule elastic collisions a source of heat in some regions in case C.

To summarise our discussion on the impact of $D^+ - D_2$ elastic collisions on the energy and momentum balance, analysis suggests that for the chosen set of plasma-neutral interactions included, as the temperatures approach 1 eV in these simulations, plasma-neutral energy/momentum exchange weakens significantly between the start of the detached region and the target through all channels except $D^+ - D_2$ elastic collisions:

- Comparison of case A and B shows that ion-molecule elastic collisions are necessary to observe a significant drop in temperature below 1 eV
- In case C, even though ion-molecule elastic collisions are present, their impact on $q_{||,\text{i,int}}$ weak and a significant drop in temperature below 1 eV is not observed

The weak impact of ion-molecule elastic collisions in case C could be due to the following:

- Fewer ions and molecules—fewer interactions and less energy exchange
- Almost half the plasma across the detached region is nitrogen, this could weaken the impact of ion-molecule interactions in two ways:
  1. Nitrogen is seven times heavier than deuterium. The presence of a large amount of nitrogen results in $q_{||,\text{i,kin}} > q_{||,\text{i,int}}$ across the detached region, which we hypothesise weakens the impact of ion-molecule elastic collisions on $q_{||,\text{i,int}}$. The nitrogen essentially acts as a momentum reservoir.
  2. Since molecules do not interact with nitrogen which makes up almost half the plasma, their impact on heat dissipation and temperature is weakened—the nitrogen also acts as a 'temperature' reservoir.

3.3.4. Impact of $D^+ - D_2$ elastic collisions on divertor n_e profiles. We have now seen that the access to sub-eV temperatures through $D^+ - D_2$ elastic collisions near the target in

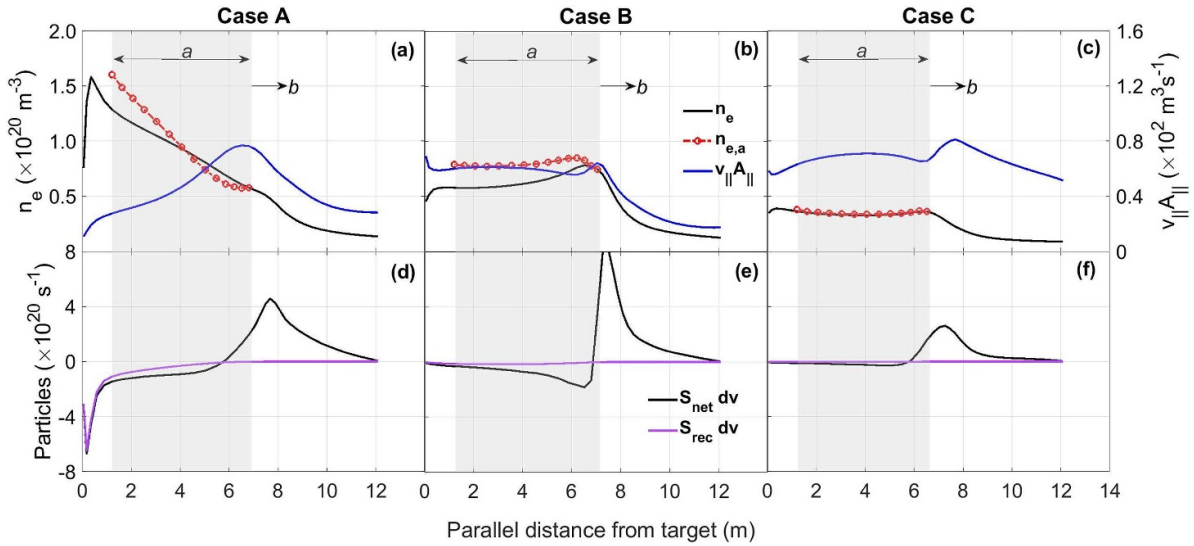

Figure 11. Particle balance analysis across the detached region for each case. Figures (*a*)–(*c*) show the electron density profile, and the product of the parallel flow velocity and flux tube cross-section area. The net particle sink and the recombination sink are shown in figures (*d*)–(*f*), equation (4) is applied in the grey region where the $S_{\rm net}$ is relatively small. It can be seen that the qualitative features of $n_{\rm e}$ are reproduced by equation (4) which shows that the increase in density across the divertor in case A is due to $D^+ - D_2$ interactions driving a strong reduction in $v_{||}$,

case A is an important factor that results in high recombination levels in this case. However, the higher density near the target in this case also significantly enhances the recombination levels. In fact, an important observation in this comparison is that there is a qualitative difference between the density profile in case A and that in case C. In case A, the density increases significantly across the detached region and peaks close to the target whereas in case C, there is little change in the density across the detached region. While turning off $D^+ - D_2$ elastic collisions leads to higher temperatures near the target, it also results in a density profile that is mostly flat across most of the detached region as in case C and thus lower densities near the target. In this last part of our discussion on $D^+ - D_2$ elastic collisions, we will describe the impact of these elastic collisions on the divertor density profiles.

The $n_{\rm e}$ profile as a function of the parallel distance from the target is shown for each case in figures 11(*a*)–(*c*). It can be seen that between the start of the detached region and 1 m from the target (shown in grey), there is a slight increase in $n_{\rm e}$ in case C and a small drop in case B, but the profiles remain mostly flat. But in case A, $n_{\rm e}$ increases strongly across this region (by $\approx$120%).

The reason for the observed difference can be understood as follows: the density profile along a single flux tube is determined by the net particle source and the flow velocity. If we consider point *a* to be anywhere between 1 m from the target and the start of the detached region, and point *b* to be at the start of the detached region, then according to particle balance, the electron density at *a*, $n_{{\rm e},a}$, is related to that at *b*, $n_{{\rm e},b}$, through $v_{||}$ and the cross-sectional areas ($A_{||}$) at those points, and the net particle source ($S_{n,{\rm net}}$) integrated between those points:

$$n_{{\rm e},a} = \frac{n_{{\rm e},b} v_{||,b} A_{||,b} + \int_a^b S_{n,{\rm net}} {\rm d}V}{v_{||,a} A_{||,a}}. \tag{4}$$

In figures 11(*d*)–(*f*), the $S_{\rm rec}$ profiles and the net volumetric particle source profiles, $S_{n,{\rm net}}$ are shown for each case. Firstly, it can be seen that in all cases, $S_{n,{\rm net}}$ is relatively small across most of the grey region—if $S_{n,{\rm net}} \approxeq 0$ between *a* and *b*, then equation (4) becomes

$$n_{{\rm e},a} \approxeq \frac{n_{{\rm e},b} v_{||,b} A_{||,b}}{v_{||,a} A_{||,a}}. \tag{5}$$

Equation (5) suggests that $n_{{\rm e},a} > n_{{\rm e},b}$ if the product $v_{||,a}A_{||,a} > v_{||,b}A_{||,b}$ (and vice-versa). Profiles of $v_{||}A_{||}$ as a function of parallel distance from the target are shown in figures 11(*a*)–(*c*)—these correspond to $v_{||,a}A_{||,a}$ in the grey region and $v_{||,b}A_{||,b}$ at point *b*. Across the grey region, $v_{||}A_{||}$ drops dramatically (by over $\approx$60%) in case A and changes by less than 10% in the other two cases. These changes are consistent with changes in the density. In fact, the $v_{||}$ and $A_{||}$ profiles are indeed sufficient to reproduce the qualitative features of the density profiles in the grey region, $n_{{\rm e},a}$, also shown in figures 11(*a*)–(*c*). Since the simulation geometry is the same in all cases, the $A_{||}$ profile between *a* and *b* (or anywhere) is also the same. The differences in the n_e profiles across the grey region must therefore result primarily from differences in the $v_{||}$ profile in that region. Figure 11 demonstrates that the significant increase in n_e observed across the detached region in case A is primarily a result of a corresponding reduction in $v_{||}$, and that ion-molecule elastic collisions are necessary for this strong reduction to occur. A similar reduction in $v_{||}$ is not observed in case C even though ion-molecule elastic collisions are included here, which is again because of the large impurity fraction. As seen in figure 9, most of the momentum in case C is carried by N^+; because the plasma across the detached region in case C is a lot heavier than that in case A, even a similar reduction in the dynamic pressure in both cases will

lead to a relative smaller reduction in the flow velocity in the case with the heavier plasma.

In summary, ion-molecule elastic collisions essentially 'plug' the plasma flow across the detached region in case A, leading to a density profile that is strongly peaked near the target. However, this 'plugging' of the plasma flow is not as efficient in case C because there are fewer molecules and also because the seven times heavier nitrogen makes up a significant portion of the plasma, resulting in a relatively flat density profile.

4. Summary and conclusions

In this study, the SOLPS-ITER code package was used to perform a deuterium fuelling scan and a nitrogen seeding scan (at a constant fuelling rate) in the MAST-U Super-X geometry and obtain strongly detached solutions. The aim was to carry out a detailed comparison of conditions when the divertor is strongly detached due to a high upstream density to those when it is a result of significantly increased impurity radiation at a relatively low upstream density. The key difference between the two scans was in the role of EIR in the reduction of the particle flux to the target. In the seeding scan, the reduction in particle flux was primarily due to a reduction in the divertor ionisation source with EIR playing a negligible role. In contrast, EIR was found to play a key role in target particle flux reduction in the fuelling scan. This was due to a combination of lower ($\leqslant 1$ eV) temperatures near the target and higher divertor plasma densities achieved in the fuelling scan compared to the seeding scan. Further, we observed a qualitative difference in the divertor density profiles of the most strongly detached solutions obtained in the two scans. While the density in the fuelling case increased significantly across the divertor, peaking near the target, the divertor density profile in the nitrogen seeded case was mostly flat. Qualitative features of the strongly detached solution from the seeded case (higher temperatures, flat divertor density profile and therefore negligible recombination) were recovered in the fuelling scan by turning off $D^+ - D_2$ elastic collisions and repeating the scan, demonstrating that this interaction is necessary to access strongly recombining conditions in the fuelling scan for the simulated parameter space. In order to better understand the role of $D^+ - D_2$ elastic collisions, a strongly detached case was chosen from each of the three scans and an energy, momentum and particle balance analysis was performed on each case.

Analysis of the fuelling cases showed that important heat dissipation mechanisms like impurity radiation and hydrogenic excitation/ionisation weaken significantly as the temperatures approach 1 eV and $D^+ - D_2$ elastic collisions play the key role in removing heat from the plasma to access sub-eV temperatures required for EIR conditions. Energy and momentum loss to $D^+ - D_2$ elastic collisions are enhanced as a result of higher divertor plasma and neutral densities which lead to more plasma-neutral interactions. Interestingly, both the increase in plasma density across the detached region and the increase in the D_2 density near the target in case A are a result of how $D^+ - D_2$ elastic collisions affect the energy and momentum balance. A relatively large plasma flux flows into the detached region and towards the target while interacting with a relatively dense cloud of deuterium atoms and molecules. Primarily through $D^+ - D_2$ elastic collisions, this cloud 'plugs' the plasma flow across the detached region. Due to a relatively small net particle sink across most of the detached region, we observe a steady increase in plasma density across this region. These interactions also appear to keep most of the molecules 'squashed' to the target, as indicated by the sharp increase in molecular density close to the target. Coupled with the already high plasma density, this sharp increase in molecule density close to the target drives strong power losses to $D^+ - D_2$ elastic collisions, leading to sub-eV temperatures and increased EIR across this region.

The plasma flux entering the detached region in the seeded case is half that in the fuelling case, and it interacts with a neutral cloud of significantly lower ($\times 5$) density. In addition, singly ionised nitrogen makes up almost half the plasma across the detached region and therefore carries a large fraction of the plasma momentum because of its mass. Most of the momentum lost by D^+ fluid through interaction with neutrals is regained through friction with the N^+ fluid. The N^+ fluid essentially 'drags' the divertor plasma through a relatively low neutral density cloud, without interacting with any of the neutrals in these simulations. The combined result of a heavy plasma flowing through a low density neutral cloud is that the plasma flow is not 'plugged' as effectively as in the fuelling case—the reduction in plasma flow velocity across the divertor is therefore not as strong compared to that in the fuelling case. Again, the net particle source is small across most of the detached region, and the relatively small changes in the flow velocity across the detached region result in a flat density profile. As in the fuelling case, the molecules are 'squashed' close the target in the seeded case as well—the molecule density increases sharply close to the target. While this increase in molecule density is indeed accompanied by an increase in power losses to $D^+ - D_2$ elastic collisions in the seeded case, this is not as strong and the temperature in this case does not drop significantly below 1 eV. The lower plasma and neutral densities correspond to fewer plasma-neutral interactions and therefore lower heat dissipation. Further, the presence of a large amount nitrogen could weaken the actual impact of $D^+ - D_2$ elastic collisions on the internal energy in two ways. First, $D^+ - D_2$ elastic collisions appear to preferentially dissipate directed kinetic energy as opposed to internal energy. The large amount of nitrogen results in the plasma having a significantly higher directed kinetic energy, weakening the impact of the elastic collisions on the internal energy. Second, all ion species have the same temperature and since nitrogen ions do not interact with neutrals in our simulations, they can only 'lose' heat through friction with the main ions (radiative losses are small because of the low temperature). The nitrogen

therefore acts like a reservoir of heat which again results in $D^+ - D_2$ elastic collisions having a rather weak impact on the plasma internal energy. Thus, the plasma temperature across the detached region does not drop significantly below 1 eV. The combined result of a relatively low plasma density and a high plasma temperature is negligible EIR.

The increased connection length of the Super-X between the *X*-point and target enables the thermal front to move quite far from the target in each case. A common feature in each of the cases considered here is that the particle source is small across a significant portion of the detached region, and through particle balance, the density profile across most of the detached region in each case depends on how plasma-neutral momentum exchange affects the plasma flow profile along the field. This analysis suggests that in strongly detached conditions in the simulated parameter space, elastic collisions between ions and neutrals can introduce a drag on the plasma flowing across the detached region towards the target, which can affect the divertor plasma density profile. Further, it suggests that volumetric power loss through the electron channel may weaken significantly as the temperature in the divertor falls below 1 eV, leaving ion channel power losses, particularly elastic collisions, to dominate at these temperatures. In our simulations, $D^+ - D_2$ elastic collisions primarily introduce the drag on the plasma in both the seeded and non-seeded cases, but their weak impact on the nitrogen heavy divertor plasma appears to be primarily what leads to the observed differences between the two cases. In reality, other energy and momentum removal mechanisms, not considered in our simulations, will also be present in nitrogen seeded scenarios—interactions with nitrogen molecules and ammonia chemistry—included in the AMMONX scheme [30], not used in these simulations. Therefore, it is possible that the densities in our seeded case may be underestimated, and the temperatures may be overestimated. In other words, it is possible that such qualitative differences in strongly detached conditions achieved from either method may not necessarily be observed in experiment. Although results on TCV and C-MOD suggest that there is a difference, the size of this effect remains to be seen.

At least for the chosen set of plasma-neutral interactions, it appears that the impurity concentration across the rather large detached region of the Super-X can be significantly higher than that in the radiating thermal front region. Since radiating impurities are significantly heavier than deuterium, in strongly detached conditions (i.e. when the thermal front is far from the target), a relatively small impurity fraction may carry a significant amount of the plasma momentum across the detached region. In reactor relevant conditions, heavy noble gases will likely be used for power dissipation. Therefore, key energy and momentum exchange channels for these impurity ions and neutrals need to be identified in order to accurately model strongly detached SXD conditions involving large impurity fractions. We further note that the rates used for deuterium ion conversion in these simulations may need to be updated, this could result in MAR playing a more significant role in target particle flux reduction. We have not included particle drifts and SOL currents and not used the AMMONX scheme in these simulations. Finally, further work may be needed to identify suitable boundary conditions to accommodate the high impurity fraction solution studied here. Ideally, future work investigates the impact of including the additional physics discussed above.

Acknowledgments

This work has been part-funded by the EPSRC Energy Programme (Grant Number EP/W006839/1]). To obtain further information on the data and models underlying this paper please contact PublicationsManager@ukaea.uk. This work has also received funding from the University of York and the research by B. Lipschultz was funded in part by the Wolfson Foundation and UK Royal Society through a Royal Society Wolfson Research Merit Award as well as by the RCUK Energy Programme (EPSRC Grant Number EP/I501045).

Appendix. Role of $D^+ - D_2$ interactions in $q_{||,\mathrm{i,kin}}$ dissipation

As mentioned earlier, since $q_{||,\mathrm{i,kin}}$ and P_{dyn} are closely related, the momentum loss decomposition (figures 7(*j*)–(*l*)) can be used to infer which process dissipates $q_{||,\mathrm{i,kin}}$. It should be noted that this is only valid in regions where P_{stat} is mostly constant because the momentum sinks shown do not necessarily always correspond to P_{dyn} dissipation. To calculate exactly how much $q_{||,\mathrm{i,kin}}$ is dissipated by $D^+ - D_2$ interactions, we first identify the region across which there is little change in P_{stat}: this is between $\approx 2\,\mathrm{m} - 5\,\mathrm{m}$ in case A and $\approx 0\,\mathrm{m} - 5\,\mathrm{m}$ in case C. Since the net momentum loss, momentum loss due to $D^+ - D_2$ interactions and the total change in $q_{||,\mathrm{i,kin}}$ are known, the fraction of momentum lost to this interaction can be used to calculate the contribution of this interaction in $q_{||,\mathrm{i,kin}}$ dissipation. The fraction of the total P_{dyn} dissipated, $\int_a^b S_{P_{\mathrm{dyn,tot}}}\mathrm{d}v$, by ion-molecule interactions, $\int_a^b S_{P_{\mathrm{dyn,mol}}}\mathrm{d}v$, between the downstream end of the region where the P_{stat} is roughly constant, point a, and the upstream end of this region, point b, is equal to the fraction of the total $q_{||,\mathrm{i,kin}}$ dissipated across this region, $\int_a^b S_{\mathrm{kin,tot}}\mathrm{d}v = q_{||,\mathrm{i,kin},b} - q_{||,\mathrm{i,kin},a}$, by ion-molecule interactions $\int_a^b S_{\mathrm{kin,mol}}\mathrm{d}v$:

$$\frac{\int_a^b S_{P_{\mathrm{dyn,mol}}}\mathrm{d}V}{\int_a^b S_{P_{\mathrm{dyn,tot}}}\mathrm{d}V} = \frac{\int_a^b S_{\mathrm{kin,mol}}\mathrm{d}V}{\int_a^b S_{\mathrm{kin,tot}}\mathrm{d}V}. \tag{A.1}$$

In other words, the amount of $q_{||,\mathrm{i,kin}}$ dissipated through ion-molecule interactions is simply:

$$\int_a^b S_{\mathrm{kin,mol}}\mathrm{d}V = (q_{||,\mathrm{i,kin},b} - q_{||,\mathrm{i,kin},a})\frac{\int_a^b S_{P_{\mathrm{dyn,mol}}}\mathrm{d}V}{\int_a^b S_{P_{\mathrm{dyn,tot}}}\mathrm{d}V}. \tag{A.2}$$

ORCID iDs

O. Myatra https://orcid.org/0000-0002-1469-2429
B. Dudson https://orcid.org/0000-0002-0094-4867

B. Lipschultz https://orcid.org/0000-0001-5968-3684
K. Verhaegh https://orcid.org/0000-0002-0500-2764

References

[1] Loarte A. *et al* 2007 Chapter 4: Power and particle control *Nucl. Fusion* **47** S203
[2] Pacher G.W., Pacher H.D., Janeschitz G., Kukushkin A.S., Kotov V. and Reiter D. 2007 Modelling of DEMO core plasma consistent with SOL/divertor simulations for long-pulse scenarios with impurity seeding *Nucl. Fusion* **47** 469–78
[3] Krasheninnikov S.I. and Kukushkin A.S. 2017 Physics of ultimate detachment of a tokamak divertor plasma *J. Plasma Phys.* **83** 155830501
[4] Dunne M.G. *et al* 2017 The role of the density profile in the ASDEX-Upgrade pedestal structure *Plasma Phys. Control. Fusion* **59** 014017
[5] Neuhauser J. *et al* 1995 The compatibility of high confinement times and complete divertor detachment in ASDEX-Upgrade *Plasma Phys. Control. Fusion* **37** A37–A51
[6] Asakura N., Nakano T., Oyama N., Sakamoto T., Matsunaga G. and Itami K. 2009 Investigations of impurity seeding and radiation control for long-pulse and high-density H-mode plasmas in JT-60U *Nucl. Fusion* **49** 115010
[7] Maddison G.P. *et al* 2011 Moderation of divertor heat loads by fuelling and impurity seeding in well-confined ELMy H-mode plasmas on JET *Nucl. Fusion* **51** 042001
[8] Reinke M.L. *et al* 2011 Effect of N2, Ne and Ar seeding on Alcator C-Mod H-mode confinement *J. Nucl. Mater.* **415** S340–4
[9] Kallenbach A. *et al* 2015 Partial detachment of high power discharges in ASDEX Upgrade *Nucl. Fusion* **55** 053026
[10] Wang H.Q., Guo H.Y., Petrie T.W., Leonard A.W., Thomas D.M. and Watkins J.G. 2017 Effects of low-Z and high-Z impurities on divertor detachment and plasma confinement *Nucl. Mater. Energy* **12** 1–6
[11] Huber A. *et al* 2020 Peculiarity of highly radiating multi-impurity seeded H-mode plasmas on JET with ITER-like wall *Phys. Scr.* **2020** 014055
[12] Bernert M. *et al* 2021 X-point radiation, its control and an ELM suppressed radiating regime at the ASDEX Upgrade tokamak *Nucl. Fusion* **61** 024001
[13] Eldon D. *et al* 2021 An analysis of controlled detachment by seeding various impurity species in high performance scenarios on DIII-D and EAST *Nucl. Mater. Energy* **27** 100963
[14] Siccinio M., Fable E., Angioni C., Saarelma S., Scarabosio A. and Zohm H. 2018 Impact of an integrated core/SOL description on the R and B T optimization of tokamak fusion reactors *Nucl. Fusion* **58** 016032
[15] Loarte A. and Neu R. 2017 Power exhaust in tokamaks and scenario integration issues *Fusion Eng. Des.* **122** 256–73
[16] Soukhanovskii V.A. 2017 A review of radiative detachment studies in tokamak advanced magnetic divertor configurations *Plasma Phys. Control. Fusion* **59** 64005
[17] Kallenbach A., Bernert M., Dux R., Casali L., Eich T. and Giannone L. 2013 Impurity seeding for tokamak power exhaust : from present devices via ITER to DEMO *Plasma Phys. Control Fusion* **55** 124041
[18] Havlíčková E., Fundamenski W., Subba F., Coster D., Wischmeier M. and Fishpool G. 2013 Benchmarking of a 1D scrape-off layer code SOLF1D with SOLPS and its use in modelling long-legged divertors *Plasma Phys. Control. Fusion* **55** 065004
[19] Havlíčková E., Wischmeier M., Lipschultz B. and Fishpool G. 2015 The effect of the Super-X divertor of MAST Upgrade on impurity radiation as modelled by SOLPS *J. Nucl. Mater.* **463** 1209–13
[20] Havlíčková E. *et al* 2015 SOLPS analysis of the MAST-U divertor with the effect of heating power and pumping on the access to detachment in the Super-x configuration *Plasma Phys. Control. Fusion* **57** 115001
[21] Moulton D., Lipschultz B. and Harrison J. 2017 Detachment onset in MAST-U according to SOLPS-ITER *44th EPS Conf. on Plasma Physics(EPS) 2017* pp 1–45 (available at: http://ocs.ciemat.es/EPS2017PAP/pdf/O5.129.pdf)
[22] Lipschultz B. *et al* 1999 The role of particle sinks and sources in Alcator C-Mod detached divertor discharges *Phys. Plasmas* **6** 1907
[23] Verhaegh K. *et al* 2019 An improved understanding of the roles of atomic processes and power balance in divertor target ion current loss during detachment *Nucl. Fusion* **59** 126038
[24] Goetz J.A. *et al* 1999 High confinement dissipative divertor operation on Alcator C-Mod *Phys. Plasmas* **6** 1899
[25] Verhaegh K. *et al* 2021 The role of plasma-molecule interactions on power and particle balance during detachment on the TCV tokamak *Nucl. Fusion* **61** 106014
[26] Schneider R. *et al* 2006 Plasma edge physics with B2-Eirene *Contrib. Plasma Phys.* **46** 3–191
[27] Janev R. K.R.D. 2018 Isotope effects in molecule assisted recombination and dissociation in divertor plasmas *Technical Report* (Jülich: Forschungszentrum Jülich GmbH)
[28] Verhaegh K. *et al* 2023 Investigating the impact of the molecular charge-exchange rate on detached SOLPS-ITER simulations *Nucl. Fusion* **63** 7
[29] Reiter D. The data file AMJUEL: additional atomic and molecular data for EIRENE (available at: www.researchgate.net/publication/228728483_The_data_file_AMJUEL_Additional_atomic_and_molecular_data_for_EIRENE)
[30] Touchard S., Mougenot J., Rond C., Hassouni K. and Bonnin X. 2019 Ammonx: a kinetic ammonia production scheme for eirene implementation *Nucl. Mater. Energy* **18** 12–17
[31] Smolders A. *et al* 2020 Comparison of high density and nitrogen seeded detachment using solps-iter simulations of the tokamaká configuration variable *Plasma Phys. Control. Fusion* **62** 125006
[32] Kirk A. *et al* 2004 A comparison of mid-plane scrape-off-layer measurements with model predictions in MAST and the calculation of cross-field transport coefficients *Plasma Phys. Control. Fusion* **46** 1591–603
[33] Harrison J.R., Fishpool G.M. and Kirk A. 2013 L-mode and inter-ELM divertor particle and heat flux width scaling on MAST *J. Nucl. Mater.* **438** S375–8
[34] Thornton A.J. and Kirk A. 2014 Scaling of the scrape-off layer width during inter-ELM H modes on MAST as measured by infrared thermography *Plasma Phys. Control. Fusion* **56** 055008
[35] Février O. *et al* 2020 Nitrogen-seeded divertor detachment in TCV l-mode plasmas *Plasma Phys. Control. Fusion* **62** 035017
[36] Hutchinson I. 1994 Thermal front analysis of detached divertors and MARFEs *Nucl. Fusion* **34** 1337–48
[37] Lipschultz B., Parra F.I. and Hutchinson I.H. 2016 Sensitivity of detachment extent to magnetic configuration and external parameters *Nucl. Fusion* **56** 056007
[38] Kukushkin A.S., Krasheninnikov S.I., Pshenov A.A. and Reiter D. 2017 Role of molecular effects in divertor plasma recombination *Nucl. Mater. Energy* **12** 984–8